5

Equilibrium Shape of Crystals

T.L. Einstein

DEPARTMENT OF PHYSICS AND CONDENSED MATTER THEORY CENTER, UNIVERSITY OF MARYLAND, COLLEGE PARK, MD, USA

CHAPTER OUTLINE

215

5.1 Introduction

The notion of equilibrium crystal shape (ECS) is arguably the platonic ideal of crystal growth and underpins much of our thinking about crystals. Accordingly, it has been the subject of several special reviews and tutorials [1–4,215] and is a prominent part of most volumes and extended review articles and texts about crystals and their growth [5–9]. In actual situations, there are many complications that thwart observation of such behavior, including kinetic barriers, impurities, and other bulk defects like dislocations. Furthermore, the notion of a well-defined equilibrium shape requires that there is no contact of the crystal with a wall or surface, since that would alter its shape. By the same token, the crystal cannot then be supported, so gravity is neglected. For discussions of the effect of gravity or contact with walls, see, e.g., Ref. [7].

Gibbs [10] is generally credited with being the first to recognize that the equilibrium shape of a substance is that which, for a fixed volume, minimizes the (orientation-dependent) surface free energy integrated over the entire surface; the bulk free energy is irrelevant since the volume is conserved, while edge or corner energies are ignored as being higher order effects that play no role in the thermodynamic limit. Herring [11,12] Surveys the early history in detail: The formulation of the problem was also carried out independently by Ref. [13]. The solution of this ECS problem, the celebrated Wulff construction, was stated by Ref. [14]; but his proof was incorrect. Correct proofs were subsequently given by Ref. [15–17], who presented a critical review. However, these proofs, while convincing of the theorem, were not general (and evidently applied only to $T = 0$, since they assumed the ECS to be a polyhedron and, compared the sum over the facets of the surface free energy of each facet times its area with a similar sum over a similar polyhedron with the same facet planes but slightly different areas (and the same volume)). Dinghas [18] showed that the Brunn–Minkowski inequality could be used to prove directly that any shape differing from that resulting from the Wulff construction has a higher surface free energy. Although Dinghas again considered only a special class of polyhedral shapes, Herring [11,12] completed the proof by noting that Dinghas' method is easily extended to arbitrary shapes, since the inequality is true for convex bodies in general. In their seminal paper on crystal growth, Burton, Cabrera, and Frank [19] present a novel proof of the theorem in two dimensions (2D).

Since equilibrium implies minimum Helmholtz free energy for a given volume and number, and since the bulk free energy is ipso facto independent of shape, the goal is to determine the shape that minimizes the integrated surface free energy of the crystal. The prescription takes the following form: One begins by creating a polar plot of the surface free energy as a function of orientation angle (of the surface normal) and draws a perpendicular plane (or line in 2D) through the tip of each ray. (There are many fine reviews of this subject in Refs [20–23].) Since the surface free energy in three dimensions (3D) is frequently denoted by γ, this is often called a γ plot. The shape is then the formed by the interior envelope of these planes or lines, often referred to as a pedal. At zero

temperature, when the free energy is just the energy, this shape is a polyhedron in 3D and a polygon in 2D, each reflecting the symmetry of the underlying lattice. At finite temperature, the shapes become more complex. In 2D, the sharp corners are rounded. In 3D, the behavior is richer, with two possible modes of evolution with rising temperature. For what Wortis terms type-A crystals, all sharp boundaries smooth together, while in type-B, first the corners smooth, then above a temperature denoted T_0, the edges also smooth. The smooth regions correspond to thermodynamic rough phases, with height–height correlation functions that diverge for large lateral separation l—like l^α, with α (typically $0 < \alpha < 1$) called the roughening exponent—in contrast to facets, where they attain some finite value as $l \to \infty$ [5]. The faceted regions in turn correspond to "frozen" regions. Pursuing the correspondence, sharp and smooth edges correspond to first-order and second-order phase transitions, respectively.

The aim of this chapter is primarily to explore physical ideas regarding ECS and the underlying Wulff constructions. This topic has also attracted considerable interest in the mathematics community. Readers interested in more formal and sophisticated approaches are referred to two books, Refs [24,25] and to many articles, including [26–36]. Particular attention is devoted to the origin of sharp edges on the ECS, the impact of reconstructed or adsorbed surface phases coexisting with unadorned phases, and the role and nature of possible attractive stepestep interactions.

5.2 From Surface Free Energies to Equilibrium Crystal Shape

5.2.1 General Considerations

To examine this process more closely, we examine the free energy expansion for a vicinal surface, that is, a surface misoriented by some angle θ from a facet direction. Cf. Figure 5.1. Unfortunately, this polar angle is denoted by ϕ in much of the literature on vicinal surfaces, with θ used for in-plane misorientation; most reviews of ECS use θ for the polar angle, as we shall here. The term *vicinal* implies that the surface is in the vicinity of the orientation. It is generally assumed that the surface orientation itself is rough (while the facet direction is below its roughening temperature and so is smooth). We consider the projected surface free energy $f_p(\theta,T)$ [37] (with the projection being onto the low-index reference, facet direction of terraces):

$$f_p(\theta, T) = f_0(T) + \beta(T)\frac{|\tan\theta|}{h} + g(T)\left|\tan\theta\right|^3 + c(\tan\theta)^4. \tag{5.1}$$

The first term is the surface free energy per area of the terrace (facet) orientation; it is often denoted σ. The average density of steps (the inverse of their mean separation $\langle\ell\rangle$) is $\tan\theta/h$, where h is the step height. In the second term, $\beta(T)$ is the line tension or free energy per length of step formation. (Since 2D is a dimension smaller than 3D, one uses β rather than γ. Skirting over the difference in units resulting from the dimensional
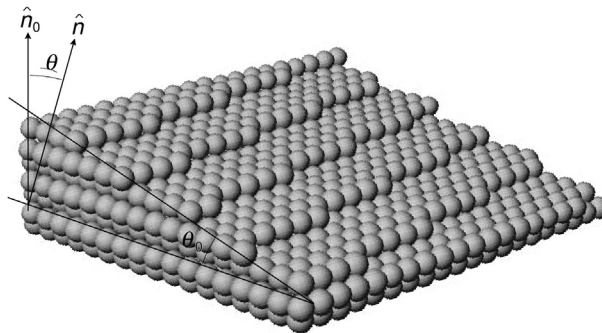
FIGURE 5.1 Portion of a $(3,\bar{2},16)$ surface, vicinal to an fcc (001), to illustrate a misoriented, vicinal surface. The vicinal surface and terrace normals are $\hat{n} = (3,-2,16)/\sqrt{269}$ and $\hat{n} = (0,0,1)$, respectively. The polar angle θ [with respect to the (001) direction], denoted ϕ in the original figure (consistent with most of the literature on vicinal surfaces), is across $(16/\sqrt{269})$, while azimuthal angle φ (denoted θ in most of the literature on vicinal surfaces), indicating how much $\hat{n}$ is rotated around $\hat{n}_0$ away from the vertical border on which θ_0 is marked, is clearly $\arctan(1/5)$; $\tan\theta_0 = \tan\theta_0\cos\phi$. Since h is $a_1/\sqrt{2}$, where a_1 is the nearest-neighbor spacing, the mean distance ℓ (in a terrace plane) between steps is $a_1/(\sqrt{2}\tan\theta) = 8\sqrt{2/13}a_1 = 3.138a_1$. While the average distance from one step to the next along a principal, (110) direction looks like $3.5a_1$, it is in fact $a_1/(\sqrt{2}\tan\theta_0) = 3.2a_1$. The "projected area" of this surface segment, used to compute the surface free energy f_p, is the size of a (001) layer: $20a_1 \times 17a_1 = 340a_1^2$; the width is $20a_1$. In "Maryland notation" (see text), z is in the $\hat{n}_0$ direction, while the normal to the vicinal, $\hat{n}$, lies in the x–z plane and y runs along the mean direction of the edges of the steps. In most discussions, $\phi = 0$, so that this direction would be that of the upper and lower edges of the depicted surface. *Adapted from Ref. [38].*

difference, many use γ in both cases.) While step free energy per length and line tension are equivalent for these systems, where the surface is at constant (zero) charge, they are inequivalent in electrochemical systems, where it is the electrode potential conjugate to the surface charge that is held fixed [39]. The third term is associated with interactions between steps, in this case assumed to be proportional to ℓ^{-2} (so that this term, which also includes the ℓ^{-1} density of steps, goes like ℓ^{-3}). The final term is the leading correction.

The ℓ^{-2} interaction is due to a combination (not a simple sum) of two repulsive potential energies: the entropic repulsion due to the forbidden crossing of steps and the elastic repulsions due to dipolar strains near each step. An explicit form for $g(T)$ is given in Eqn (5.27) below. The ℓ^{-2} of the entropic interaction can be understood from viewing the step as performing a random walk in the direction between steps (the x direction in "Maryland notation"[1] as a function of the y direction (which is timelike in the fermion transcription to be discussed later), cf. Figure 5.1, so the distance (y) it must go until it touches a neighboring step satisfies $\ell^2 \propto y$. To get a crude understanding of the origin of the elastic repulsion, one can imagine that since a step is unstable relative to a flat surface, it will try to relax toward a flatter shape, pushing atoms away from the location of the step by a distance decaying with distance from the step. When two steps are close

[1]This term was coined by a speaker at a workshop in Traverse City in August 1996—see Ref. [43] for the proceedings—and then used by several other speakers.

to each other, such relaxation will be frustrated because atoms on the terrace this pair of steps are pushed in opposite directions, so they relax less than if the steps are widely separated, leading to a repulsive interaction. Analyzed in more detail [7,40,41], this repulsion is dipolar and so proportional to ℓ^{-2}. However, attempts to reconcile the prefactor with the elastic constants of the surface have met with limited success. The quartic term in Eqn (5.1) is due to the leading (ℓ^{-3}) correction to the elastic repulsion [42], a dipole-quadrupole repulsion. It generally has no significant consequences but is included to show the leading correction to the critical behavior near a smooth edge on the ECS, to be discussed below.

The absence of a quadratic term in Eqn (5.1) reflects that there is no ℓ^{-1} interaction between steps. In fact, there are some rare geometries, notably vicinals to (110) surfaces of fcc crystals (Au in particular) that exhibit what amounts to ℓ^{-1} repulsions, which lead to more subtle behavior [44]. Details about this fascinating idiosyncratic surface are beyond the scope of this chapter; readers should see the thorough, readable discussion by van Albada et al. [45].

As temperature increases, $\beta(T)$ decreases due to increasing entropy associated with step-edge excitations (via the formation of kinks). Eventually, $\beta(T)$ vanishes at a temperature T_R associated with the roughening transition. At and above this T_R of the facet orientation, there is a profusion of steps, and the idea of a vicinal surface becomes meaningless. For rough surfaces, the projected surface free energy $f_p(\theta,T)$ is quadratic in $\tan\theta$. To avoid the singularity at $\theta = 0$ in the free energy expansion that thwarts attempts to proceed analytically, some treatments, notably Bonzel and Preuss [46], approximate $f_p(\theta,T)$ as quadratic in a small region near $\theta = 0$. It is important to recognize that the vicinal orientation is thermodynamically rough, even though the underlying facet orientation is smooth. The two regions correspond to incommensurate and commensurate phases, respectively. Thus, in a rough region, the mean spacing $\langle\ell\rangle$ between steps is not in general simply related to (i.e., an integer multiple plus some simple fraction) the atomic spacing.

Details of the roughening process have been reviewed by Weeks [216] and by van Beijeren and Nolden [9]; the chapter by Akutsu in this Handbook provides an up-to-date account. However, for use later, we note that much of our understanding of this process is rooted in the mapping between the restricted body-centered (cubic) solid-on-solid (BCSOS) model and the exactly solvable [47,48] symmetric 6-vertex model [49], which has a transition in the same universality class as roughening. This BCSOS model is based on the BCC crystal structure, involving square net layers with ABAB stacking, so that sites in each layer are lateral displaced to lie over the centers of squares in the preceding (or following) layer. Being an SOS model means that for each column of sites along the vertical direction, there is a unique upper occupied site, with no vacancies below it or floating atoms above it. Viewed from above, the surface is a square network with one pair of diagonally opposed corners on A layers and the other pair on B layers. The restriction is that neighboring sites must be on adjacent layers (so that their separation is the distance from a corner to the center of the BCC lattice). There are then six possible

configurations: two in which the two B corners are both either above or below the A corners and four in which one pair of catercorners are on the same layer and the other pair are on different layers (one above and one below the first pair). In the symmetric model, there are three energies, $-\epsilon$ for the first pair, and $\pm\delta/2$ for the others, the sign depending on whether the catercorner pair on the same lattice is on A or B [50]. The case $\delta = 0$ corresponds to the F-model, which has an infinite-order phase transition and an essential singularity at the critical point, in the class of the Kosterlitz-Thouless [51] transition [52]. (In the "ice" model, ϵ also is 0.) For the asymmetric 6-vertex model, each of the six configurations can have a different energy; this model can also be solved exactly [53,54].

5.2.2 More Formal Treatment

To proceed more formally, we largely follow [1]. The shape of a crystal is given by the length $R(\widehat{\mathbf{h}})$ of a radial vector to the crystal surface for any direction $\widehat{\mathbf{h}}$. The shape of the crystal is defined as the thermodynamic limit of this crystal for increasing volume V, specifically.

$$r\left(\widehat{\mathbf{h}}, T\right) \equiv \lim_{V \to \infty} \left[R\left(\widehat{\mathbf{h}}\right) \Big/ \alpha V^{1/3}\right], \tag{5.2}$$

where α is an arbitrary dimensionless variable. This function $r(\widehat{\mathbf{h}}, T)$ corresponds to a free energy. In particular, since both independent variables are fieldlike (and so intrinsically intensive), this is a Gibbs-like free energy. Like the Gibbs free energy, $r(\widehat{\mathbf{h}}, T)$ is continuous and convex in $\widehat{\mathbf{h}}$.

The Wulff construction then amounts to a Legendre transformation[2] to $r(\widehat{\mathbf{h}}, T)$ from the orientation $\widehat{\mathbf{m}}$-dependent interfacial free energy $f_i(\widehat{\mathbf{m}}, T)$ (or in perhaps the more common but less explicit notation, $\gamma(\widehat{\mathbf{m}}, T)$, which is $f_p(\theta, T)/\cos(\theta)$. For liquids, of course, $f_i(\widehat{\mathbf{m}}, T)$ is spherically symmetric, as is the equilibrium shape. Herring [12] mentions rigorous proofs of this problem by Schwarz in 1884 and by Minkowski in 1901. For crystals, $f_i(\widehat{\mathbf{m}}, T)$ is not spherically symmetric but does have the symmetry of the crystal lattice. For a system with cubic symmetry, one can write

$$f_i\left(\widehat{\mathbf{m}}, T\right) = \gamma_0(T)\left[1 + a(T)\left(m_x^4 + m_y^4 + m_z^4\right)\right], \tag{5.3}$$

where $\gamma_0(T)$ and $a(T)$ are constants. As illustrated in Figure 5.2, for $a = 1/4$ the asymmetry leads to minor distortions, which are rather inconsequential. However, for

---

[2]As exposited clearly in Ref. [55], one considers a [convex] function $y = y(x)$ and denotes its derivative as $p = \partial y/\partial x$. If one then tries to consider p instead of x as the independent variable, there is information lost: one cannot reconstruct $y(x)$ uniquely from $y(p)$. Indeed, $y = y(p)$ is a first-order differential equation, whose integration gives $y = y(x)$ only to within an undetermined integration constant. Thus, $y = y(p)$ corresponds to a family of displaced curves, only one of which is the original $y = y(x)$. The key concept is that the locus of points satisfying $y = y(x)$ can be equally well represented by a family of lines tangent to $y(x)$ at all x, each with a y-intercept ψ determined by the slope p at $(x, y(x))$. That is, $\psi = \psi(p)$ contains all the information of $y = y(x)$. Recognizing that $p = (y - \psi)/(x - 0)$, one finds the transform $\psi = y - px$. Readers should recall that this is the form of the relationship between thermodynamic functions, particularly the Helmholtz and the Gibbs free energies.
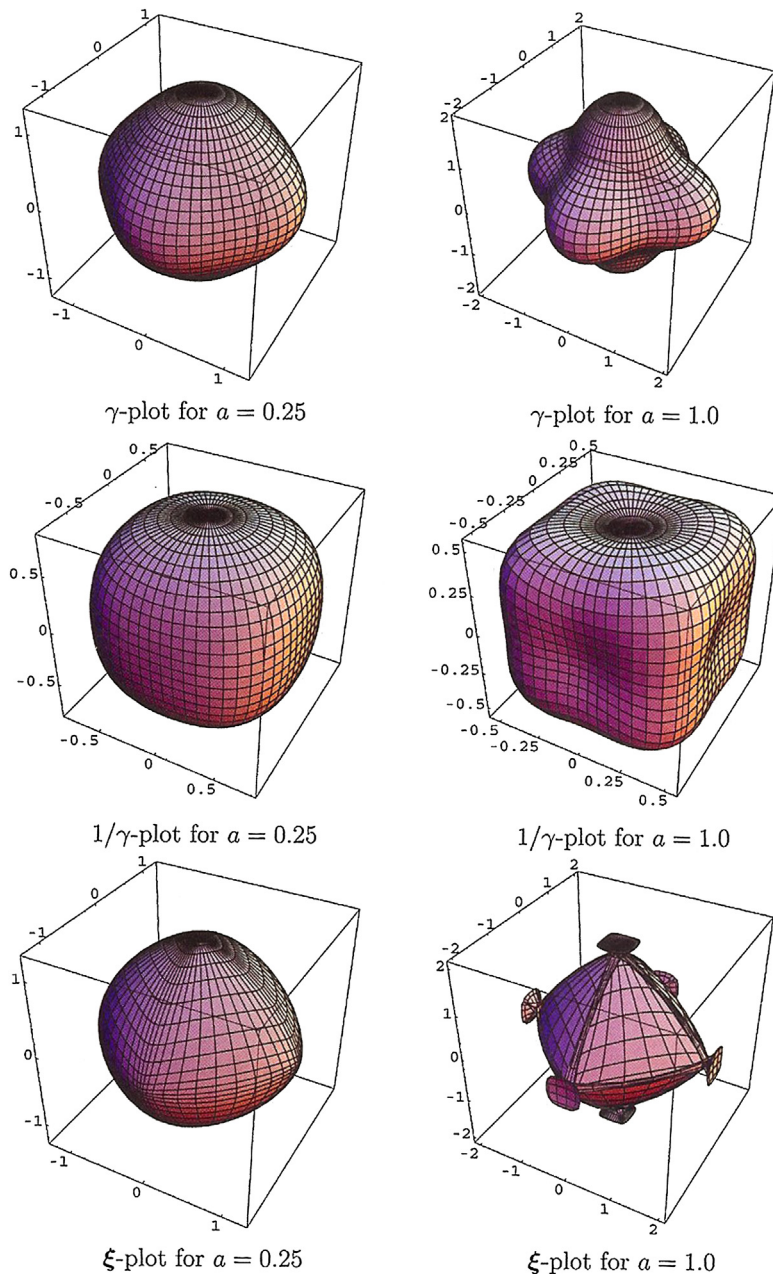
FIGURE 5.2 γ-plots (plots of $f_i(\widehat{\mathbf{m}})$, $1/\gamma$-plots and ξ-plots for Eqn (5.3) for positive values of a). For $a = 1/4$, all orientations appear on the ECS. For $a = 1.0$, the $1/\gamma$-plot has concave regions, and the ξ-plot has ears and flaps that must be truncated to give the ECS essentially an octahedron with curved faces. *From Ref. [8]*, which shows in a subsequent figure that the γ- and $1/\gamma$-plots for $a = -0.2$ and -0.5 resemble the $1/\gamma$- and γ-plots, respectively, for $a = 1/4$ and 1.

$a = 1$, the enclosed region is no longer convex, leading to an instability to be discussed shortly.

One considers the change in the interfacial free energy associated with changes in shape. The constraint of constant volume is incorporated by subtracting from the change in the integral of $f_i(\widehat{\mathbf{m}}, T)$ the corresponding change in volume, multiplied by a Lagrange multiplier λ. Herring [11,12] showed that this constrained minimization problem has a unique and rather simple solution that is physically meaningful in the limit that it is satisfactory to neglect edge, corner, and kink energies in $f_i(\widehat{\mathbf{m}}, T)$, that is, in the limit of large volume. In this case $\lambda \propto V^{-1/3}$; by choosing the proportionality constant as essentially the inverse of α, we can write the result as

$$r\left(\widehat{\mathbf{h}}, T\right) = \min_{\widehat{\mathbf{m}}} \left(\frac{f_i\left(\widehat{\mathbf{m}}, T\right)}{\widehat{\mathbf{m}} \cdot \widehat{\mathbf{h}}} \right) \tag{5.4}$$

The Wulff construction is illustrated in Figure 5.3. The interfacial free energy $f_i(\widehat{\mathbf{m}})$, at some assumed T is displayed as a polar plot. The crystal shape is then the interior envelope of the family of perpendicular planes (lines in 2D) passing through the ends of the radial vectors $\widehat{\mathbf{m}} f_i(\widehat{\mathbf{m}})$. Based on Eqn (5.4) one can, at least in principle, determine $\widehat{\mathbf{m}}(\widehat{\mathbf{h}})$ or $\widehat{\mathbf{h}}(\widehat{\mathbf{m}})$, which thus amounts to the equation of state of the equilibrium crystal shape. One can also write the inverse of Eqn (5.4):

$$\frac{1}{f_i\left(\widehat{\mathbf{m}}, T\right)} = \min_{\widehat{\mathbf{m}}} \left(\frac{1/f_i\left(\widehat{\mathbf{h}}, T\right)}{\widehat{\mathbf{m}} \cdot \widehat{\mathbf{h}}} \right) \tag{5.5}$$
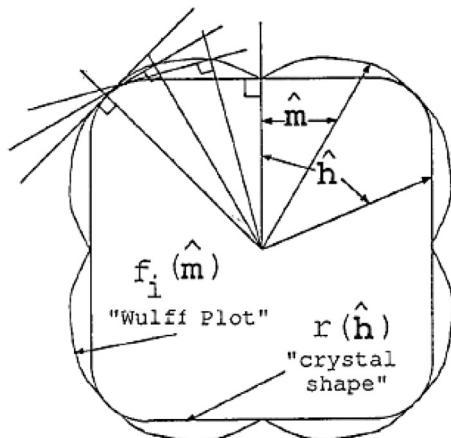
FIGURE 5.3 Schematic of the Wulff construction. The interfacial free energy per unit area $f_i\widehat{\mathbf{m}}$ is plotted in polar form (the "Wulff plot" or "γ-plot"). One draws a radius vector in each direction $\widehat{\mathbf{m}}$ and constructs a perpendicular plane where this vector hits the Wulff plot. The interior envelope of the family of "Wulff planes" thus formed, expressed algebraically in Eqn (5.4), is the crystal shape, up to an arbitrary overall scale factor that may be chosen as unity. *From Ref. [1].*

Thus, a Wulff construction using the inverse of the crystal shape function yields the inverse free energy.

To be more explicit, consider the ECS in Cartesian coordinates $z(x,y)$, i.e., $\hat{\mathbf{h}} \propto (x, y, z(x, y))$, assuming (without dire consequences [1]) that $z(x,y)$ is single-valued. Then, for any displacement to be tangent to $\hat{\mathbf{h}}$, $dz - p_x\, dx - p_y\, dy = 0$

$$\hat{\mathbf{h}} = \frac{1}{\sqrt{1 + p_x^2 + p_y^2}} \left(-p_x z, -p_y z, 1 \right), \tag{5.6}$$

where p_x is shorthand for $\partial z/\partial x$.

Then the total free energy and volume are

$$F_i(T) = \iint f_p(p_x, p_y)\, dx\, dy$$
$$V = \iint z(x, y)\, dx\, dy \tag{5.7}$$

where f_p, which incorporates the line-segment length, is $f_p \equiv [1 + p_x^2 + p_y^2]^{1/2} f_i$. Minimizing F_i subject to the constraint of fixed V leads to the Euler–Lagrange equation

$$\frac{\partial}{\partial x} \frac{f_p(\partial_x z, p_y)}{p_x} + \frac{\partial}{\partial y} \frac{f_p(p_x, p_y)}{p_y} = -2\lambda \tag{5.8}$$

(Actually, one should work with macroscopic lengths, then divide by the $V^{1/3}$ times the proportionality constant. Note that this leaves p_x and p_y unchanged [1].) On the right-hand side, 2λ can be identified as the chemical potential μ, so that the constancy of the left-hand side is a reflection of equilibrium. Equation (5.8) is strictly valid only if the derivatives of f_p exist, so one must be careful near high-symmetry orientations below their roughening temperature, for which facets occur. To show that this highly nonlinear second-order partial differential equation with unspecified boundary conditions is equivalent to Eqn (5.4), we first note that the first integral of Eqn (5.8) is simply

$$z - x p_x - y p_y = f_p(p_x, p_y) \tag{5.9}$$

The right-hand side is just a function of derivatives, consistent with this being a Legendre transformation. Then, differentiating yields

$$x = -\partial f_p \big/ \partial(p_x), \quad y = -\partial f_p \big/ \partial(p_y) \tag{5.10}$$

Hence, one can show that

$$z(x, y) = \min_{p_x, p_y} \left(f_p(p_x, p_y) + x p_x + y p_y \right) \tag{5.11}$$

5.3 Applications of Formal Results

5.3.1 Cusps and Facets

The distinguishing feature of Wulff plots of faceted crystals compared to liquids is the existence of (pointed) cusps in $f_i(\widehat{\mathbf{m}}, T)$, which underpin these facets. The simplest way to see why the cusp arises is to examine a square lattice with nearest-neighbor bonds having bond energy ϵ_1, often called a 2D Kossel [56,57] crystal; note also [210]. In this model, the energy to cleave the crystal is the Manhattan distance between the ends of the cut; i.e., as illustrated in Figure 5.4, the energy of severing the bonds between $(0,0)$ and (X,Y) is just $+\epsilon_1 (|X| + |Y|)$. The interfacial area, i.e., length, is $2(X^2 + Y^2)$ since the cleavage creates *two* surfaces. At $T = 0$, entropy plays no role, so that

$$f_i(\theta) = \frac{\epsilon_1}{2}(|\sin \theta| + |\cos\theta|) \sim \frac{\epsilon_1}{2}(1 + |\theta| + \ldots) \tag{5.12}$$

At finite T fluctuations and attendant entropy do contribute, and the argument needs more care. Recalling Eqn (5.1), we see that if there is a linear cusp at $\theta = 0$, then

$$f_i(\theta, T) = f_i(0, T) + B(T)|\theta|, \tag{5.13}$$

where $B = \beta(T)/h$, since the difference between $f_i(\theta)$ and $f_p(\theta)$ only appears at order θ^2. Comparing Eqns (5.12) and (5.13), we see that for the Kossel square $f_i(0,0) = \epsilon_1/2$ and $B(0) = \epsilon_1/2$. Further discussion of the 2D $f_i(\theta)$ is deferred to Section 5.4.3 below.

To see how a cusp in $f_i(\widehat{\mathbf{m}}, T)$ leads to a facet in the ECS, consider Figure 5.5: the Wulff plane for $\theta \gtrsim 0$ intersects the horizontal $\theta = 0$ plane at a distance $f_i(0) + d(\theta)$ from the vertical axis. The crystal will have a horizontal axis if and only if $d(\theta)$ does not
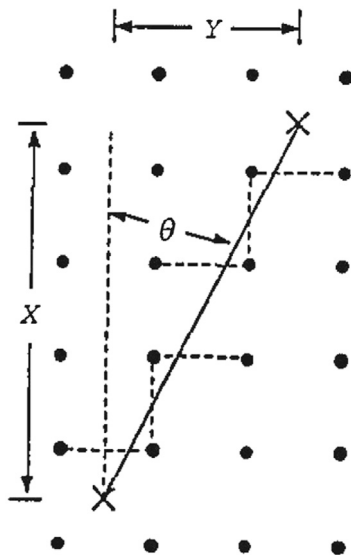

FIGURE 5.4 Kossel crystal at $T = 0$. The energy to cleave the crystal along the depicted slanted. Interface (tan $\theta = Y/Z$) is $\epsilon_1 (|X| + |Y|)$. *From Ref. [1].*
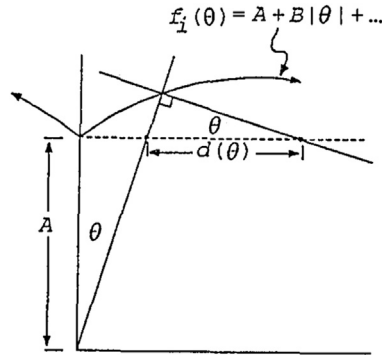
FIGURE 5.5 Wulff plot with a linear cusp at $\theta = 0$. If $d(\theta) \to 0$ as $\theta \to 0$, then there is no facet corresponding to $\theta = 0$, and the $\theta = 0$ Wulff plane (dotted line) is tangent to the crystal shape at just a single point. Since $d(\theta) = B$, a cusp in the Wulff plot leads to a facet of the corresponding orientation on the equilibrium crystal shape. *From Ref. [1].*

vanish as $\theta \to 0$. From Figure 5.5, it is clear that $\theta \approx \sin \theta \approx B\theta / d(\theta)$ for θ near 0, so that $d(0) = B > 0$. For a weaker dependence on θ, e.g., $B|\theta|^\zeta$ with $\zeta > 1$, $d(0) = 0$, and there is no facet. Likewise, at the roughening temperature, β vanishes and the facet disappears.

5.3.2 Sharp Edges and Forbidden Regions

When there is a sharp edge (or corner) on the ECS $r(\widehat{\mathbf{h}}, T)$, Wulff planes with a range of orientations $\widehat{\mathbf{m}}$ will not be part of the inner envelope determining this ECS; they will lie completely outside it. There is no portion of the ECS whose surface tangent has these orientations. As in the analogous problems with forbidden values of the "density" variable, the free energy $f_i(\widehat{\mathbf{m}}, T)$ is actually not properly defined for forbidden values of $\widehat{\mathbf{m}}$; those unphysical values should actually be removed from the Wulff plot. Figure 5.6 depicts several possible ECSs and their associated Wulff plots. It is worth emphasizing that, in the extreme case of the fully faceted ECS at $T = 0$, the Wulff plot is simply a set of discrete points in the facet directions.

Now if we denote by $\widehat{\mathbf{m}}_+$ and $\widehat{\mathbf{m}}_-$, the limiting orientations of the tangent planes approaching the edge from either side, then all intermediate values do not occur as stable orientations. These missing, not stable, "forbidden" orientations are just like the forbidden densities at liquid–gas transitions, forbidden magnetizations in ferromagnets at $T < T_c$ [58], and miscibility gaps in binary alloys. Herring [11,12] first presented an elegant way to determine these missing orientations using a spherical construction. For any orientation $\widehat{\mathbf{m}}$, this tangent sphere (often called a Herring sphere) passes through the origin and is tangent to the Wulff plot at $f_i(\widehat{\mathbf{m}})$. From geometry, he invoked the theorem that an angle inscribed in a semicircle is a right angle. Thence, if the orientation $\widehat{\mathbf{m}}$ appears on the ECS, it appears at an orientation that points outward along the radius of that sphere. Herring then observes that only if such a sphere lies completely inside the plot of $f_i(\widehat{\mathbf{m}})$ does that orientation appear on the ECS. If some part were inside, its Wulff
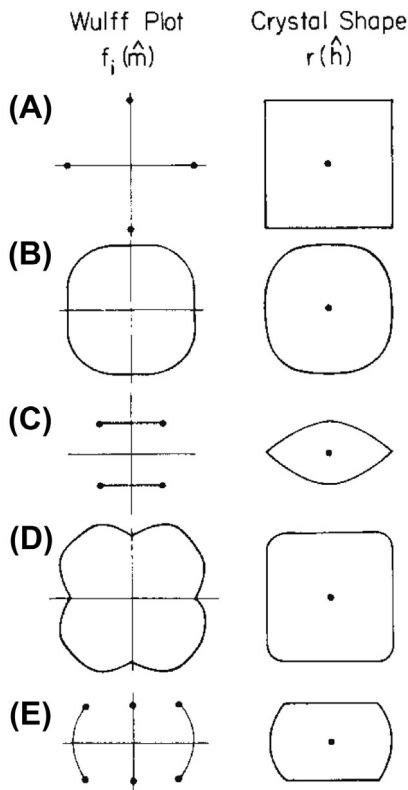
FIGURE 5.6 Some possible Wulff plots and corresponding equilibrium crystal shapes. Faceted and curved surfaces may appear, joined at sharp or smooth edges in a variety of combinations. *From Ref. [4]; the equilibrium crystal shape are also in Ref. [12].*

plane would clip off the orientation of the point of tangency, so that orientation would be forbidden.

The origin of a hill-and-valley structure from the constituent free energies [59,221,222] is illustrated schematically in Figure 5.7. It arises when they satisfy the inequality

$$f_i\left(\widehat{\mathbf{m}} = \mathbf{n}_1\right)A_1 + f_i(\mathbf{n}_2)A_2 < f_i(\mathbf{n})A, \tag{5.14}$$

where A_1 and A_2 are the areas of strips of orientation $\mathbf{n}_1$ and $\mathbf{n}_2$, respectively, while A is the area of the sum of these areas projected onto the plane bounded by the dashed lines in the figure. This behavior, again, is consistent with the identification of the misorientation as a density (or magnetizationlike) variable rather than a fieldlike one.

The details of the lever rule for coexistence regimes were elucidated by Wortis [1]: As depicted in Figure 5.8, which denotes as P and Q the two orientations bounding the region that is not stable, the lever rule interpolations lie on segments of a spherical surface. Let the edge on the ECS be at R. Then an interface created at a forbidden $\widehat{\mathbf{m}}$ will
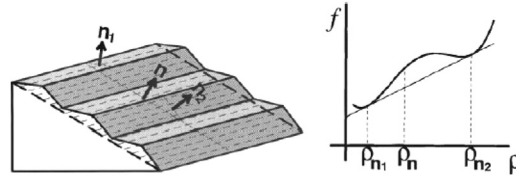
FIGURE 5.7 Illustration of how orientational phase separation occurs when a "hill-and-valley" structure has a lower total surface free energy per area than a flat surface as in Eqn (5.14). The sketch of the free energy versus $\rho \equiv \tan\theta$ shows that this situation reflects a region with negative convexity which is accordingly not stable. The dashed line is the tie bar of a Maxwell or double-tangent construction. The misorientations are the coexisting slatlike planes, with orientations $\mathbf{n}_1$ and $\mathbf{n}_2$, in the hill-and-valley structure. *From Ref. [59].*
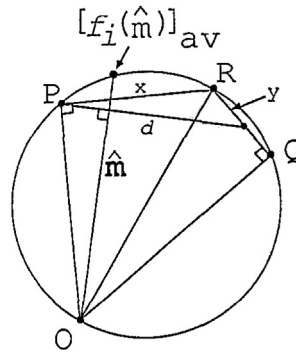

FIGURE 5.8 Equilibrium crystal shape (ECS) analogue of the Maxwell double-tangent construction. O is the center of the crystal. Points P and Q are on the (stable) Wulff plot, but the region between them is unstable; hence, the ECS follows PRQ and has an edge at R. An interface at the intermediate orientation $\widehat{\mathbf{m}}$ breaks up into the orientations P and Q with relative proportions x:y; thus, the average free energy per unit area is given by Eqn (5.15), which in turn shows that $f_i(\widehat{\mathbf{m}})_{\text{avr}}$ lies on the circle. *From Ref. [1].*

evolve toward a hill-and-valley structure with orientations P and Q with a free energy per area of

$$\left[f_i\left(\widehat{\mathbf{m}}\right) \right]_{\text{avr}} = \frac{x f_i(P) + y f_i(Q)}{d}. \tag{5.15}$$

It can then be shown that $\widehat{\mathbf{m}}[f_i(\widehat{\mathbf{m}})]_{\text{avr}}$ lies on the depicted circle, so that the Wulff plane passes through the edge at R.

5.3.3   Experiments on Lead Going beyond Wulff Plots

To determine the limits of forbidden regions, it is more direct and straightforward to carry out a polar plot of $1/f_i(\widehat{\mathbf{m}})$ [20] rather than $f_i(\widehat{\mathbf{m}})$, as discussed in Sekerka's review chapter [8]. Then a sphere passing through the origin becomes a corresponding plane; in particular, a Herring sphere for some point becomes a plane tangent to the plot of $1/f_i(\widehat{\mathbf{m}})$. If the Herring sphere is inside the Wulff plot, then its associated plane lies outside the plot of $1/f_i(\widehat{\mathbf{m}})$. If, on the other hand, if some part of the Wulff plot is inside a
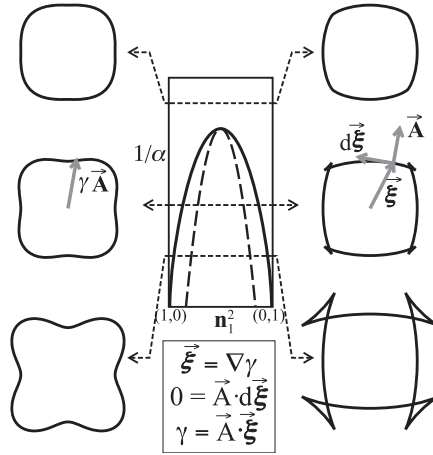
FIGURE 5.9 Graphical constructions for an anisotropic $f_i(\widehat{\mathbf{m}})$ for various values of an anisotropy parameter α, where $f_i \propto 1 + \alpha\cos^2\theta\sin^2\theta$. In the left column $f_i(\theta)$ is plotted from top to bottom for $\alpha = 1/2, 1, 2$. Anisotropy increases with positive α, so $1/\alpha$ corresponds in some sense to a temperature in conventional plots. In the center panel, $\mathbf{n}_1^2$ is $\cos^2\theta$. The shape resulting from the gradient construction with the ears removed is the Wulff equilibrium crystal shape. *From Ref. [60].*

Herring sphere, the corresponding part of the $1/f_i(\widehat{\mathbf{m}})$ plot will be outside the plane. Thus, if the plot of $1/f_i(\widehat{\mathbf{m}})$ is convex, all its tangent planes will lie outside, and all orientations will appear on the ECS. If it is not convex, it can be made so by adding tangent planes. The orientations associated with such tangent planes are forbidden, so their contact curve with the $1/f_i(\widehat{\mathbf{m}})$ plot gives the bounding stable orientations into which forbidden orientations phase separate.

Summarizing the discussion in Ref. [8], the convexity of $1/f_i(\widehat{\mathbf{m}})$ can indeed be determined analytically since the curvature $1/f_i(\widehat{\mathbf{m}})$ is proportional (with a positive-definite proportionality constant) to the stiffness, i.e., in 2D, $\gamma + \partial^2\gamma/\partial\theta^2 = \tilde{\gamma}$, or preferably $\beta + \partial^2\beta/\partial\theta^2 = \tilde{\beta}$ as in Eqn (5.1) to emphasize that the stiffness and (step) free energy per length have different units in 2D from 3D. Hence, $1/f_i(\widehat{\mathbf{m}})$ is not convex where the stiffness is negative. The very complicated generalization of this criterion to 3D is made tractable via the ξ-vector formalism of Refs [30,61], where $\xi = \nabla(r\, f_i(\widehat{\mathbf{m}}))$, where r is the distance from the origin of the γ plot. Thus,

$$f_i(\widehat{\mathbf{m}}) = \xi \cdot \widehat{\mathbf{m}}, \quad \widehat{\mathbf{m}} \cdot d\xi = 0, \tag{5.16}$$

which is discussed well by Refs [8,62]. To elucidate the process, we consider just the 2D case [60].

The solid curve in Figure 5.10 is the ξ plot and the dashed curve is the $1/\gamma$-plot for $f_i(\widehat{\mathbf{m}}) \equiv \gamma \propto 1 + 0.2\cos 4\theta$. For this case, the $1/\gamma$-plot is not convex and the ξ plot forms "ears." The equilibrium shape is given by the interior envelope of the ξ plot; in this case it exhibits four corners.
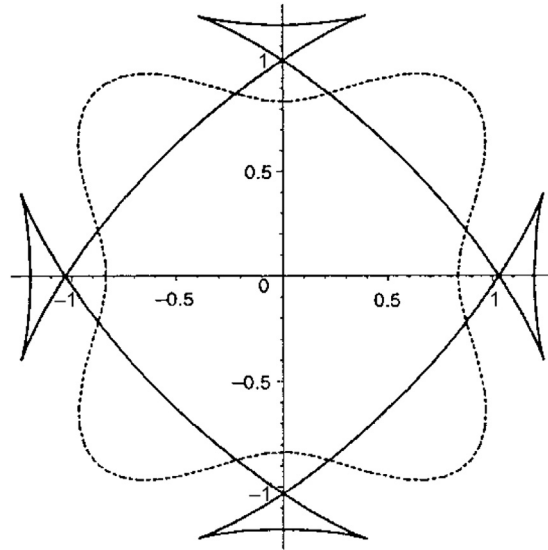
FIGURE 5.10 The solid curve is the ξ plot, while the dashed curve is the $1/\gamma$-plot for $f_i(\widehat{m}) \equiv \gamma \propto 1 + 0.2 \cos 4\,\theta$. For this case (but not for small values of *a*), the $1/\gamma$-plot is not convex, and the ξ plot forms "ears." These ears are then removed, so that the equilibrium shape is given by the interior envelope of the ξ plot, in this case having four corners. *From Ref. [62].*

Pursuing this analogy, we see that if one cleaves a crystal at some orientation $\widehat{\mathbf{m}}$ that is not on the ECS, i.e., between $\widehat{\mathbf{m}}_+$ and $\widehat{\mathbf{m}}_-$, then this orientation will break up into segments with orientations $\widehat{\mathbf{m}}_+$ and $\widehat{\mathbf{m}}_-$ such that the net orientation is still $\widehat{\mathbf{m}}$, providing another example of the lever rule associated with Maxwell double-tangent constructions for the analogous problems. The time to evolve to this equilibrium state depends strongly on the size of energy barriers to mass transport in the crystalline material; it could be exceedingly long. To achieve rapid equilibration, many nice experiments were performed on solid hcp ^{4}He bathed in superfluid ^{4}He, for which equilibration occurs in seconds [63–66], and many more (see Ref. [67] for a comprehensive recent review). Longer but manageable equilibration times are found for Si and for Au, Pb, and other soft transition metals.

5.4 Some Physical Implications of Wulff Constructions

5.4.1 Thermal Faceting and Reconstruction

A particularly dramatic example is the case of surfaces vicinal to Si (111) by a few degrees. In one misorientation direction, the vicinal surface is stable above the reconstruction temperature of the (111) facet, but below that temperature, $f_i(111)$ decreases significantly so that the original orientation is no longer stable and phase separates into reconstructed (111) terraces and more highly misoriented segments [68,69]. The

correspondence to other systems with phase separation at first-order transitions is even more robust. Within the coexistence regime, one can in mean field determine a spinodal curve. Between it and the coexistence boundary, one observes phase separation by nucleation and growth, as for metastable systems; inside the spinodal, one observes much more rapid separation with a characteristic most-unstable length [70]. This system is discussed further below.

Wortis [1] describes "thermal faceting" experiments in which metal crystals, typically late-transition or noble metal elements like Cu, Ag, and Fe, are cut at a high Miller index direction and polished. They are then annealed at high temperatures. If the initial plane is in a forbidden direction, optical striations, due to hill-and-valley formation, appear once these structures have reached optical wavelengths. While the characteristic size of this pattern continues to grow as in spinodal decomposition, the coarsening process is eventually slowed and halted by kinetic limitations.

There are more recent examples of such phenomena. After sputtering and annealing above 800 K, Au(4,5,5) at 300 K forms a hill-and-valley structure of two Au(111) vicinal surfaces, one that is reconstructed and the other not, as seen in Figure 5.11. This seems to be an equilibrium phenomenon: It is reversible and independent of cooling rate [77]. Furthermore, while it has been long known that adsorbed gases can induce faceting on bcc (111) metals [72], ultrathin metal films have also been found to produce faceting of W(111), W(211), and Mo(111) [73,74].
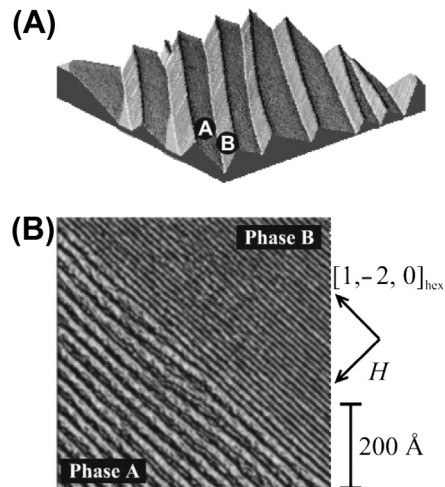
FIGURE 5.11 Morphology of the faceted Au(4,5,5) surface measured at room temperature. (A) 3D plot of a large-scale (scan area: 1.4 × 1.4 mm) scanning tunneling microscopy (STM) image. Phases A and B form the hill-and-valley morphology. (B) STM image zoomed in on a boundary between the two phases. All steps single-height, i.e., 2.35Å high. Phase B has smaller terraces, 13Å wide, while phase A terraces are about 30Å wide. This particular surface has (2,3,3) orientation. *From Ref. [71].*

5.4.2   Types A and B

The above analysis indicates that at $T = 0$, the ECS of a crystal is a polyhedron having the point symmetry of the crystal lattice, a result believed to be general for finite-range interactions [75]. All boundaries between facets are sharp edges, with associated forbidden nonfacet orientation; indeed, the Wulff plot is just a set of discrete points in the symmetry directions. At finite temperature, two possibilities have been delineated (with cautions [1], labeled nonmnemonically) A and B. In type A, there are smooth curves between facet planes rather than edges and corners. Smooth here means, of course, that not only is the ECS continuous, but so is its slope, so that there are no forbidden orientations anywhere. This situation corresponds to continuous phase transitions. In type B, in contrast, corners round at finite T but edges stay sharp until some temperature T_0. For $T_0 < T < T_1$, there are some rounded edges and some sharp edges, while above T_1 all edges are rounded.

Rottman and Wortis [4] present a comprehensive catalog of the orientation phase diagrams, Wulff plots, and ECSs for the cases of nonexistent, weakly attractive, and weakly repulsive next-nearest-neighbor (NNN) bonds in 3D. Figures 5.12 and 5.13 show the orientation phase diagrams and the Wulff plots with associated ECSs, respectively, for weakly attractive NNN bonds. As indicated in the caption, it is easy to describe what then happens when $\epsilon_2 = 0$ and only {100} facets occur. Likewise, Figures 5.14 and 5.15 show the orientation phase diagrams and the Wulff plots with associated ECSs, respectively, for weakly repulsive NNN bonds.
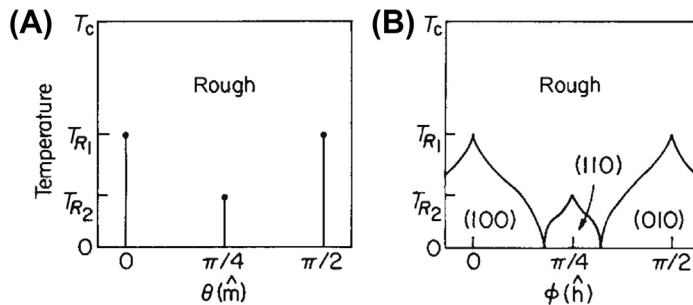
FIGURE 5.12 Interfacial phase diagrams for simple-cubic nearest-neighbor Kossel crystal with nearest-neighbor as well as (weak) next nearest-neighbor (NNN) attractions. The angular variables θ and ϕ (not to be confused with φ, cf. Section 5.2.1) interfacial orientation ($\hat{m}$) and equilibrium crystal shape ($\hat{h}$), respectively, in an equatorial section of the full 3D phase diagram. (A) The $T-\theta$ phase diagram (b) shows the locus of cusps in the Wulff plot along the symmetry directions below the respective roughening temperatures. For no NNN interaction ($\epsilon_2 = 0$), there are only cusps at vertical lines at 0 and $\pi/2$. (B) The $T - \hat{h}$ phase diagram gives the faceted areas of the crystal shape. The NNN attraction leads to additional (111) (not seen in the equatorial plane) and (110) facets at low enough temperature. Thus, for $\epsilon_2 = 0$ the two bases of the (100) and (010) phases meet and touch each other at (and only at) $\phi = \pi/4$ (at $T = 0$), with no intervening (110) phase. Each type of facet disappears at its own roughening temperature. Above the phase boundaries enclosing those regions, the crystal surfaces are smoothly curved (i.e., thermodynamically "rough"). This behavior is consistent with the observed phase diagram of hcp ^{4}He. *From Ref. [4].*

FIGURE 5.13 Representative Wulff plots and equilibrium crystal shapes for the crystal with weak next nearest-neighbor attractions whose phase diagram is shown in Figure 5.12. At low enough temperature there are (100), (110), and (111) facets. For weak attraction, the (110) and (111) facets roughen away below the (100) roughening temperature. For $\epsilon_2 = 0$, $T_{R_2} = 0$, so that the configurations in the second row do not occur; in the first row, the octagon becomes a square and the perspective shape is a cube. Facets are separated at $T > 0$ by curved surfaces, and all transitions are second order. Spherical symmetry obtains as T approaches melting at T_c. From Ref. [4].
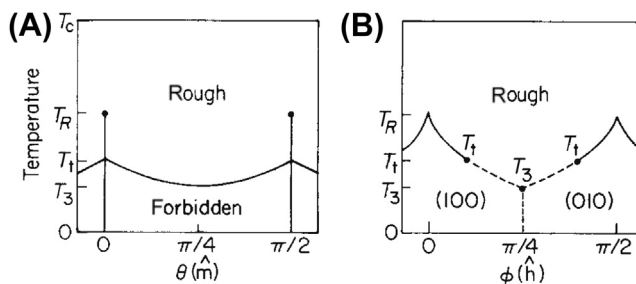
FIGURE 5.14 Interfacial phase diagram with (weak) next nearest-neighbor (NNN) repulsion rather than attraction as in Figure 5.12. The NNN repulsion stabilizes the (100) facets. Curved surfaces first appear at the cube corners and then reach the equatorial plane at T_3. The transition at the equator remains first order until a higher temperature T_t. The dotted boundaries are first order. A forbidden (coexistence) region appears in the $T - \hat{\mathbf{h}}$ phase diagram. From Ref. [4].
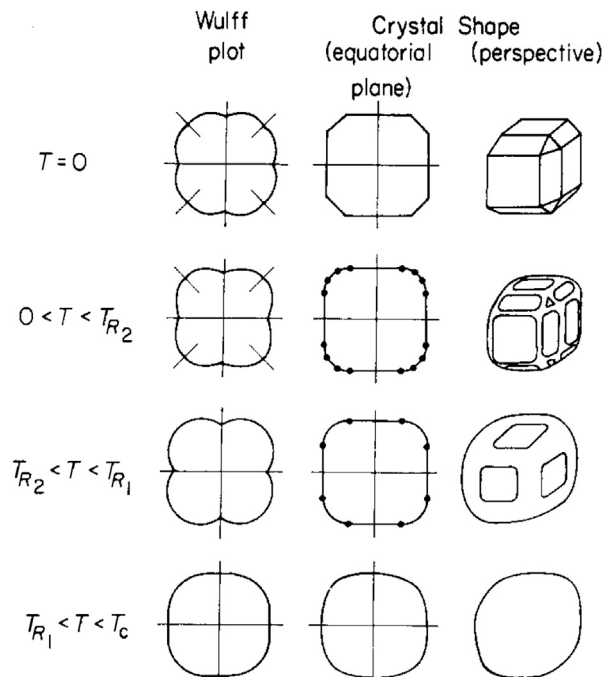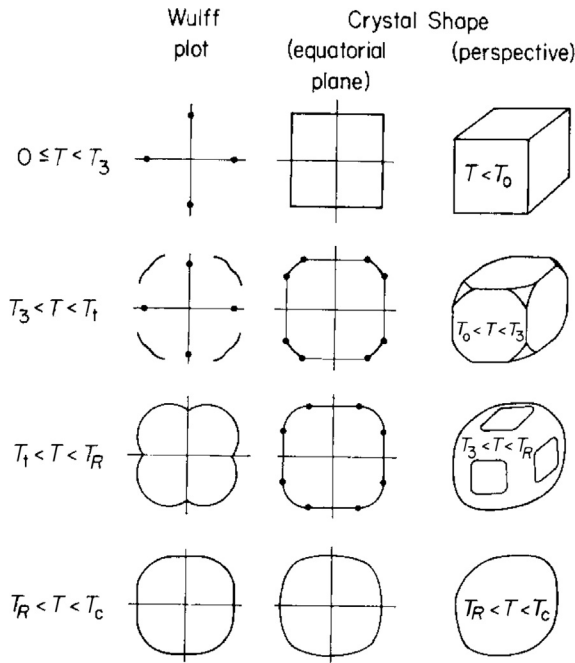
FIGURE 5.15 Representative Wulff plots and equilibrium crystal shapes for the crystal with weak next nearest-neighbor repulsions whose phase diagram is shown in Figure 5.14. Curved surfaces appear first at the cube corners. Junctions between facets and curved surfaces may be either first or second order (sharp or smooth), depending on orientation and temperature. *From Ref. [4].*

5.4.3 2D Studies

Exploring the details is far more transparent in 2D than in 3D. The 2D case is physically relevant in that it describes the shape of islands of atoms of some species at low fractional coverage on an extended flat surface of the same or another material. An entire book is devoted to 2D crystals [76]. The 2D perspective can also be applied to cylindrical surfaces in 3D, as shown by Ref. [7]. Formal proof is also more feasible, if still arduous, in 2D: An entire book is devoted to this task [25]; see also Refs [34,35].

For the 2D nearest-neighbor Kossel crystal described above [1] notes that at $T = 0$ a whole class of Wulff planes pass through a corner. At finite T, thermal fluctuations lift this degeneracy and the corner rounds, leading to type A behavior. To gain further insight, we now include a next nearest-neighbor (NNN) interaction ϵ_2, so that

$$f_i(\theta) = \frac{\epsilon_1 + \epsilon_2}{2}(|\cos\theta| + |\sin\theta|) + \frac{\epsilon_2}{2}(|\cos\theta| - |\sin\theta|) \tag{5.17}$$

For favorable NNN bonds, i.e., $\epsilon_2 > 0$, one finds new {11} facets but still type A behavior with sharp edges, while for unfavorable NNN bonds, i.e., $\epsilon_2 < 0$, there are no new facets but for finite T, the edges are no longer degenerate so that type B behavior obtains. Again recalling that $f_i(\theta) = f_p(\theta)|\cos\theta|$, we can identify $f_0 = \epsilon_2 + \epsilon_1/2$ and $\beta/h = \epsilon_1/2$, as noted in other treatments, e.g., Ref. [77]. That work, however, finds that such a model cannot adequately account for the orientation-dependent stiffness of islands on Cu(001).

Attempts to resolve this quandary using 3-site non-pairwise (trio) interactions [78,79] did not prove entirely satisfactory. In contrast, on the hexagonal Cu(111) surface, only NN interactions are needed to account adequately for the experimental data [79,80]. In fact, for the NN model on a hexagonal grid, [81] found an exact and simple, albeit implicit, expression for the ECS. However, on such (111) surfaces (and basal planes of hcp crystals), lateral pair interactions alone cannot break the symmetry to produce a difference in energies between the two kinds of step edges, viz. {100} and {111} microfacets (A and B steps, respectively, with no relation to types A and B!). The simplest viable explanation is an orientation-dependent trio interaction; calculations of such energies support this idea [79,80].

Strictly speaking, of course, there should be no 2D facet (straight edge) and accompanying sharp edges (corners) at $T > 0$ (see Refs [82–85] and references therein) since that would imply 1D long-range order, which should not occur for short-range interactions. Measurements of islands at low temperatures show edges that appear to be facets and satisfy Wulff corollaries such as that the ratio of the distances of two unlike facets from the center equals the ratio of their f_i [86]. Thus, this issue is often just mentioned in passing [87] or even ignored. On the other hand, sophisticated approximations for $f_i(\theta)$ for the 2D Ising model, including NNN bonds, have been developed, e.g., Ref. [88], allowing numerical tests of the degree to which the ECS deviates from a polygon near corners of the latter. One can also gauge the length scale at which deviations from a straight edge come into play by using that the probability per atom along the edge for a kink to occur is essentially the Boltzmann factor associated with the energy to create the kink [89].

Especially for heteroepitaxial island systems (when the island consists of a different species from the substrate), strain plays an important if not dominant role. Such systems have been investigated, e.g., by Liu [90], who points out that for such systems the shape does not simply scale with λ, presumably implying the involvement of some new length scale[s]. A dramatic manifestation of strain effects is the island shape transition of Cu on Ni(001), which changes from compact to ramified as island size increases [91]. For small islands, additional quantum-size and other effects lead to favored island sizes (magic numbers).

5.5 Vicinal Surfaces–Entrée to Rough Regions Near Facets

In the rough regions, the ECS is a vicinal surface of gradually evolving orientation. To the extent that a local region has a particular orientation, it can be approximated as an infinite vicinal surface. The direction perpendicular to the terraces (which are densely packed facets) is typically called $\hat{z}$. In "Maryland notation" (cf. Section 5.2.1) the normal to the vicinal surface lies in the x–z plane, and the distance ℓ between steps is measured along $\hat{x}$, while the steps run along the $\hat{y}$ direction. In the simplest and usual approximation, the repulsions between adjacent steps arise from two sources: an entropic or

steric interaction due to the physical condition that the steps cannot cross, since over-hangs cannot occur in nature. The second comes from elastic dipole moments due to local atomic relaxation around each step, leading to frustrated lateral relaxation of atoms on the terrace plane between two steps. Both interactions are $\propto 1/\ell^2$.

The details of the distribution $\breve{P}(\ell)$ of spacings between steps have been reviewed in many works [60,92,93,97]. The average step separation $\langle\ell\rangle$ is the only characteristic length in the $\hat{x}$ direction. N.B., $\langle\ell\rangle$ need not be a multiple of, or even simply related to, the substrate lattice spacing. Therefore, we consider $P(s) = \langle\ell\rangle^{-1}\breve{P}(\ell)$, where $s \equiv \ell/\langle\ell\rangle$, a dimensionless length. For a "perfect" cleaved crystal, $P(s)$ is just a spike $\delta(s - 1)$. For straight steps placed randomly at any position with probability $1/\langle\ell\rangle$, $P(s)$ is a Poisson distribution $\exp(-s)$. Actual steps do meander, as one can study most simply in a terrace step kink (TSK) model. In this model, the only excitations are kinks (with energy ϵ) along the step. (This is a good approximation at low temperature T since adatoms or vacancies on the terrace cost several ϵ_1 ($4\epsilon_1$ in the case of a simple-cubic lattice). The entropic repulsion due to steps meandering dramatically decreases the probability of finding adjacent steps at $\ell \ll \langle\ell\rangle$. To preserve the mean of one, $P(s)$ must also be smaller than $\exp(-s)$ for large s.

If there is an additional energetic repulsion A/ℓ^2, the magnitude of the step meandering will decrease, narrowing $P(s)$. As $A \rightarrow \infty$, the width approaches 0 ($P(s) \rightarrow \delta(s - 1)$, the result for perfect crystals). We emphasize that the energetic and entropic interactions do not simply add. In particular, there is no negative (attractive) value of A at which the two cancel each other (cf. Eqn (5.30) below.) Thus, for strong repulsions, steps rarely come close, so the entropic interaction plays a smaller role, while for $A < 0$, the entropic contribution increases, as illustrated in Figure 5.16 and explicated below. We emphasize that the potentials of both interactions decay as ℓ^{-2} (cf. Eqn (5.27)
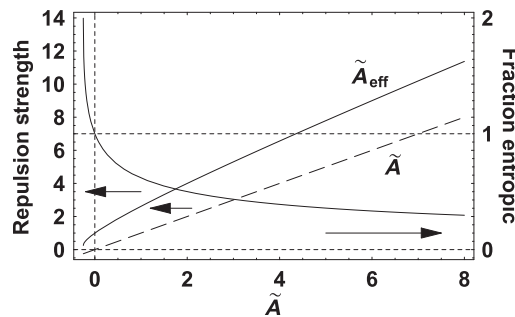
FIGURE 5.16 Illustration of how entropic repulsion and energetic interactions combine, plotted versus the dimensionless energetic interaction strength $\tilde{A} \equiv A\tilde{\beta}/(k_BT)^2$. The dashed straight line is just $\tilde{A}$. The solid curve above it is the combined entropic and energetic interactions, labeled $\tilde{A}_{\text{eff}}$ for reasons explained below. The difference between the two curves at any value of the abscissa is the dimensionless entropic repulsion for that $\tilde{A}$. The decreasing curve, scaled on the right ordinate, is the ratio of this entropic repulsion to the total dimensionless repulsion $\tilde{A}_{\text{eff}}$. It falls monotonically with $\tilde{A}$, passing through unity at $\tilde{A} = 0$. See the discussion accompanying Eqn (5.26) for more information and explicit expressions for the curves. *From Ref. [92].*

below), in contrast to some claims in the literature (in papers analyzing ECS exponents) that entropic interactions are short range while energetic ones are long range.

Investigation of the interaction between steps has been reviewed well in several places [60,94–97]. The earliest studies seeking to extract A from terrace-width distributions (TWDs) used the mean-fieldlike Gruber–Mullins [96] approximation, in which a single active step fluctuates between two fixed straight steps $2\langle \ell \rangle$ apart. Then the energy associating with the fluctuations $x(y,t)$ is

$$\Delta \mathcal{E} = -\beta(0)L_y + \int_0^{L_y} \beta(\theta(y)) \sqrt{1 + \left(\frac{\partial x}{\partial y}\right)^2} \, dy, \tag{5.18}$$

where L_y is the size of the system along the mean step direction (i.e., the step length with no kinks). We expand $\beta(\theta)$ as the Taylor series $\beta(0) + \beta'(0)\theta + \frac{1}{2}\beta''(0)\theta^2$ and recognize that the length of the line segment has increased from dy to $dy/\cos\theta \approx dy(1 + \frac{1}{2}\theta^2)$. For close-packed steps, for which $\beta'(0) = 0$, it is well known that (using $\theta \approx \tan\theta = \partial x/\partial y$)

$$\Delta \mathcal{E} \approx \frac{\tilde{\beta}(0)}{2} \int_0^{L_y} \left(\frac{\partial x}{\partial y}\right)^2 dy, \quad \tilde{\beta}(0) \equiv \beta(0) + \beta''(0), \tag{5.19}$$

where $\tilde{\beta}$ is the step stiffness [97]. N.B., the stiffness $\tilde{\beta}(\theta)$ has the same definition for steps with arbitrary in-plane orientation—for which $\beta'(\theta) \neq 0$—because to create such steps, one must apply a "torque" [98] which exactly cancels $\beta'(\theta)$. (See Refs [88,99] for a more formal proof.)

Since $x(y)$ is taken to be a single-valued function that is defined over the whole domain of y, the 2D configuration of the step can be viewed as the worldline of a particle in 1D by recognizing y as a timelike variable. Since the steps cannot cross, these particles can be described as spinless fermions in 1D, as pointed out first by de Gennes [100] in a study of polymers in 2D [220]. Thus, this problem can be mapped into the Schrödinger equation in 1D: $\partial x/\partial y$ in Eqn (5.19) becomes $\partial x/\partial t$, with the form of a velocity, with the stiffness playing the role of an inertial mass. This correspondence also applies to domain walls of adatoms on densely covered crystal surfaces, since these walls have many of the same properties as steps. Indeed, there is a close correspondence between the phase transition at smooth edges of the ECS and the commensurate-incommensurate phase transitions of such overlayer systems, with the rough region of the ECS corresponding to the incommensurate regions and the local slope related to the incommensurability [101–105]. Jayaprakash et al. [37] provide the details of the mapping from a TSK model to the fermion picture, complete with fermion creation and annihilation operators.

In the Gruber–Mullins [96] approximation, a step with no energetic interactions becomes a particle in a 1D infinite-barrier well of width $2\langle\ell\rangle$, with well-known groundstate properties:

$$\psi_0(\ell) \propto \sin\left(\frac{\pi\ell}{2\langle\ell\rangle}\right); \quad P(s) = \sin^2\left(\frac{\pi s}{2}\right); \quad E_0 = \frac{(\pi k_B T)^2}{8\tilde{\beta}\langle\ell\rangle^2} \tag{5.20}$$

Thus, it is the kinetic energy of the ground state in the quantum model that corresponds to the entropic repulsion (per length) of the step. In the exact solution for the free energy expansion of the ECS [106], the numerical coefficient in the corresponding term is 1/6 rather than 1/8. Note that $P(s)$ peaks at $s = 1$ and vanishes for $s \geq 2$.

Suppose, next, that there is an energetic repulsion $U(\ell) = A/\ell^2$ between steps. In the 1D Schrödinger equation, the prefactor of $-\partial^2 \psi(\ell)/\partial \ell^2$ is $(k_B T)^2/2\tilde{\beta}$, with the thermal energy $k_B T$ replacing $\hbar$. (Like the repulsions, this term has units ℓ^{-2}.) Hence, A only enters the problem in the dimensionless combination $\tilde{A} \equiv A\tilde{\beta}/(k_B T)^2$ [107]. In the Gruber–Mullins picture, the potential (per length) experienced by the single active particle is (with $\check{\ell} \equiv \ell - \langle \ell \rangle$)

$$\tilde{U}\left(\check{\ell}\right) = \frac{\tilde{A}}{\left(\check{\ell} - \langle \ell \rangle\right)^2} + \frac{\tilde{A}}{\left(\check{\ell} + \langle \ell \rangle\right)^2} = \frac{2\tilde{A}}{\langle \ell \rangle^2} + \frac{6\tilde{A}\check{\ell}^2}{\langle \ell \rangle^4} + \mathcal{O}\left(\frac{\tilde{A}\check{\ell}^4}{\langle \ell \rangle^6}\right) \tag{5.21}$$

The first term is just a constant shift in the energy. For $\tilde{A}$ sufficiently large, the particle is confined to a region $\left|\check{\ell}\right| \ll \langle \ell \rangle$, so that we can neglect the fixed walls and the quartic term, reducing the problem to the familiar simple harmonic oscillator, with the solution:

$$\psi_0(\ell) \propto e^{-\check{\ell}^2/4w^2}; \ P_G(s) \equiv \frac{1}{\sigma_G\sqrt{2\pi}} \exp\left[-\frac{(s-1)^2}{2\sigma_G^2}\right] \tag{5.22}$$

where $\sigma_G = (48\tilde{A})^{-1/4}$ and $w = \sigma_G \langle \ell \rangle$.

For $\tilde{A}$ of 0 or 2, the TWD can be computed exactly (See below). For these cases, Eqns (5.20) and (5.22), respectively, provide serviceable approximations. It is Eqn (5.22) that is prescribed for analyzing TWDs in the most-cited resource on vicinal surfaces [58]. Indeed, it formed the basis of initial successful analyses of experimental scanning tunneling microscopy (STM) data [108]. However, it has some notable shortcomings. Perhaps most obviously, it is useless for small but not vanishing $\tilde{A}$, for which the TWD is highly skewed, not resembling a Gaussian, and the peak, correspondingly, is significantly below the mean spacing. For large values of $\tilde{A}$, it significantly underestimates the variance or, equivalently, the value of $\tilde{A}$ one extracts from the experimental TWD width [109]: in the Gruber–Mullins approximation the TWD variance is the same as that of the active step, since the neighboring step is straight. For large $\tilde{A}$, the fluctuations of the individual steps on an actual vicinal surface become relatively independent, so the variance of the TWD is the *sum* of the variance of each, i.e., twice the step variance. Given the great (quartic) sensitivity of $\tilde{A}$ to the TWD width, this is problematic. As experimentalists acquired more high-quality TWD data, other approximation schemes were proposed, all producing Gaussian distributions with widths $\propto \tilde{A}^{-1/4}$, but with proportionality constants notably larger than $48^{-1/4} = 0.38$.

For the "free-fermion" ($\tilde{A} = 0$) case, [110] developed a sequence of analytic approximants to the exact but formidable expression [111,112] for $P(s)$. They, as well as a slightly earlier paper [113], draw the analogy between the TWD of vicinal surfaces and

the distribution of spacings between interacting (spinless) fermions on a ring, the Calogero–Sutherland model [113,114], which, in turn for three particular values of the interaction—in one case repulsive ($\tilde{A} = 2$), in another attractive ($\tilde{A} = -1/4$), and lastly the free-fermion case ($\tilde{A} = 0$)—could be solved exactly by connecting to random matrix theory [92,111,115]; Figure 5.5 of Ref. [117] depicts the three resulting TWDs.

These three cases can be well described by the Wigner surmise, for which there are many excellent reviews [111,117,118]. Explicitly, for $\varrho = 1$, 2, and 4:

$$P_\varrho(s) = a_\varrho s^\varrho \exp\left(-b_\varrho s^2\right), \tag{5.23}$$

where the subscript of P refers to the exponent of s. In random matrix literature, the exponent of s, viz. 1, 2, or 4, is called β, due to an analogy with inverse temperature in one justification. However, to avoid possible confusion with the step free energy per length β or the stiffness $\tilde{\beta}$ for vicinal surfaces, I have sometimes named it instead by the Greek symbol that looked most similar, ϱ, and do so in this chapter. The constants b_ϱ, which fixes its mean at unity, and a_ϱ, which normalizes $P(s)$, are

$$b_\varrho = \left[\frac{\Gamma\left(\frac{\varrho+2}{2}\right)}{\Gamma\left(\frac{\varrho+1}{2}\right)}\right]^2 \qquad a_\varrho = \frac{2\left[\Gamma\left(\frac{\varrho+2}{2}\right)\right]^{\varrho+1}}{\left[\Gamma\left(\frac{\varrho+1}{2}\right)\right]^{\varrho+2}} = \frac{2b_\varrho^{(\varrho+1)/2}}{\Gamma\left(\frac{\varrho+1}{2}\right)} \tag{5.24}$$

Specifically, $b_\varrho = \pi/4$, $4/\pi$, and $64/9\pi$, respectively, while $a_\varrho = \pi/2$, $32/\pi^2$, and $(64/9\pi)^3$, respectively.

As seen most clearly by explicit plots, e.g., Figure 4.2(a) of Haake's text [118], $P_1(s)$, $P_2(s)$, and $P_4(s)$ are excellent approximations of the exact results for orthogonal, unitary, and symplectic ensembles, respectively, and these simple expressions are routinely used when confronting experimental data in a broad range of physical problems [118,119]. (The agreement is particularly outstanding for $P_2(s)$ and $P_4(s)$, which are the germane cases for vicinal surfaces, significantly better than any other approximation [120].)

Thus, the Calogero–Sutherland model provides a connection between random matrix theory, notably the Wigner surmise, and the distribution of spacings between fermions in 1D interacting with dimensionless strength $\tilde{A}$. Specifically:

$$\tilde{A} = \frac{\varrho}{2}\left(\frac{\varrho}{2} - 1\right) \quad \Leftrightarrow \quad \varrho = 1 + \sqrt{1 + 4\tilde{A}}. \tag{5.25}$$

For an arbitrary system, there is no reason that $\tilde{A}$ should take on one of the three special values. Therefore, we have used Eqn (5.28) for arbitrary ϱ or $\tilde{A}$, even though there is no symmetry-based justification of distribution based on the Wigner surmise of Eqn (5.26), and refer hereafter to this formula, Eqns (5.26, 7.27), as the generalized Wigner distribution (GWD). Arguably the most convincing argument is a comparison of the predicted variance with numerical data generated from Monte Carlo simulations. See Ref. [92] for further discussion.

There are several alternative approximations that lead to a description of the TWD as a Gaussian [109]; in particular, focus on the limit of large ϱ, neglecting the entropic

interaction in that limit. The variance $\sigma^2 \propto \tilde{A}^{-1/2}$, the proportionality constant is 1.8 times that in the Gruber–Mullins case. This approximation is improved, especially for repulsions that are not extremely strong, by including the entropic interaction in an average way. This is done by replacing $\tilde{A}$ by

$$\tilde{A}_{\mathrm{eff}} = \left(\frac{\varrho}{2}\right)^2 = \tilde{A} + \frac{\varrho}{2}. \tag{5.26}$$

Physically, $\tilde{A}_{\mathrm{eff}}$ gives the full strength of the inverse-square repulsion between steps, i.e., the modification due to the inclusion of entropic interactions. Thus, in Eqn (5.1)

$$g(T) = \frac{(\pi k_B T)^2}{6h^3\tilde{\beta}}\tilde{A}_{\mathrm{eff}} = \frac{(\pi k_B T)^2}{24h^3\tilde{\beta}}\left[1 + \sqrt{1 + 4\tilde{A}}\right]^2. \tag{5.27}$$

From Eqn (5.29) it is obvious that the contribution of the entropic interaction, viz. the difference between the total and the energetic interaction, as discussed in conjunction with Figure 5.16, is $\varrho/2$. Remarkably, the ratio of the entropic interaction to the total interaction is $(\varrho/2)/(\varrho/2)^2 = 2/\varrho$; this is the fractional contribution that is plotted in Figure 5.16.

5.6 Critical Behavior of Rough Regions Near Facets

5.6.1 Theory

Assuming (cf. Figure 5.17) $\hat{\mathbf{z}}$ the direction normal to the facet and (x_0,z_0) denote the facet edge, $z \sim z_0 - (x - x_0)^\vartheta$ for $x \geq x_0$. We show that the critical exponent ϑ[3] has the value $3/2$ for the generic smooth edge described by Eqn (5.1) (with the notation of Eqn (5.13)):

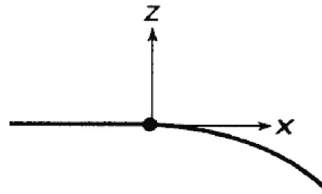$$f_p(p) = f_0 + Bp + gp^3 + cp^4. \tag{5.28}$$

FIGURE 5.17 Critical behavior of the crystal shape near a smooth (second-order) edge, represented by the dot at (x_0,z_0). The temperature is lower than the roughening temperature of the facet orientation, so that the region to the left of the dot is flat. The curved region to the right of the dot correspond to a broad range of rough orientations. In the thermodynamic limit, the shape of the smoothly curved region near the edge is described by the power law $z \sim z_0 - (x - x_0)^\vartheta$. Away from the edge there are "corrections to scaling", i.e., higher order terms (cf. Eqn (5.33)). For an actual crystal of any finite size, there is "finite-size rounding" near the edge, which smooths the singular behavior. *Adapted from Ref. [120].*

---

[3]The conventional designation of this exponent is λ or θ. However, these Greek letters are the Lagrange multiplier of the ECS and the polar angle, respectively. Hence, we choose ϑ for this exponent.

Then we perform a Legendre transformation [55] as in Refs [125,126]; explicitly:

$$\frac{f_p(p) - \tilde{f}(\eta)}{p} = \left[\frac{df_p}{dp} \equiv \eta\right] = B + 3gp^2 + 4cp^3 \tag{5.29}$$

Hence:

$$\tilde{f}(\eta) = f_0 - 2gp^3(\eta) - 3cp^4(\eta) \tag{5.30}$$

But from Eqn (5.29):

$$p = \left(\frac{\eta - B}{3g}\right)^{1/2}\left[1 - \frac{2c}{3g}\left(\frac{\eta - B}{3g}\right)^{1/2} + \ldots\right] \tag{5.31}$$

Inserting this into Eqn (5.30) gives

$$\tilde{f}(\eta) = f_0 - 2g\left(\frac{\eta - B}{3g}\right)^{3/2} + c\left(\frac{\eta - B}{3g}\right)^2 + \mathcal{O}\left(\frac{\eta - B}{3g}\right)^{5/2} \tag{5.32}$$

for $\eta \geq B$ and $\tilde{f}(\eta) = f_0$ for $\eta \leq B$. (See Refs [9,120,122].) Note that this result is true not just for the free-fermion case but even when steps interact. Jayaprakash et al. [37] further show that the same ϑ obtains when the step–step interaction decreases with a power law in ℓ that is greater than 2. We identify $\tilde{f}(\eta)$ with $r(\hat{\mathbf{h}})$, i.e., the magnetic-fieldlike variable discussed corresponds to the so-called Andreev field η. Writing $z_0 = f_0/\lambda$ and $x_0 = B/\lambda$, we find the shape profile

$$\begin{aligned}\frac{z(x)}{z_0} &= 1 - 2\left(\frac{f_0}{g}\right)^{1/2}\left(\frac{x - x_0}{z_0}\right)^{3/2} \\ &+ \frac{cf_0}{g^2}\left(\frac{x - x_0}{z_0}\right)^2 + \mathcal{O}\left(\frac{x - x_0}{z_0}\right)^{5/2}\end{aligned} \tag{5.33}$$

Note that the edge position depends only on the step free energy B, not on the step repulsion strength; conversely, the coefficient of the leading $(x - x_0)^{3/2}$ term is independent of the step free energy but varies as the inverse root of the total step repulsion strength, i.e., as $g^{-1/2}$.

If, instead of Eqn (5.31), one adopts the phenomenological Landau theory of continuous phase transitions [121] and performs an analytic expansion of $f_p(p)$ in p [123, 124] (and truncate after a quadratic term f_2p^2), then a similar procedure leads $\vartheta = 2$, which is often referred to as the "mean-field" value. This same value can be produced by quenched impurities, as shown explicitly for the equivalent commensurate-incommensurate transition by [125].

There are some other noteworthy results for the smooth edge. As the facet roughening temperature is approached from below, the facet radius shrinks like $\exp[-\pi^2 T_R/4 \{2\ln2(T_R - T)\}^{1/2}]$ [122], in striking contrast to predictions by mean field theory. The previous discussion implicitly assumes that the path along x for which $\vartheta = 3/2$ in Eqn (5.36) is normal to the facet edge. By mapping the crystal surface onto the asymmetric 6-vertex model, using its exact solution [53,54], and employing the Bethe ansatz to

expand the free energy close to the facet edge [127], find that $\vartheta = 3/2$ holds for any direction of approach along the rounded surface toward the edge, *except* along the tangential direction (the contour that is tangent to the facet edge at the point of contact x_0). In that special direction, they find the new critical exponent $\vartheta_y = 3$ (where the subscript y indicates the direction perpendicular to the edge normal, x [128]). Also, Akutsu and Akutsu [128] confirmed that this exact result was universally true for the Gruber–Mullins–Prokrovsky–Talapov free-energy expansion. (The Prokrovsky-Talapov argument was for the equivalent commensurate-incommensurate transition.) They also present numerical confirmation using their transfer-matrix method based on the product-wave-function renormalization group (PWFRG) [129,130]. Observing ϑ_y experimentally will clearly be difficult, perhaps impossible; the nature and breadth of crossover to this unique behavior has not, to the best of my knowledge, been published. A third result is that there is a jump (for $T < T_R$) in the curvature of the rounded part near the facet edge that has a universal value [106,131], distinct from the universal curvature jump of the ECS at T_R [122].

5.6.2   Experiment on Leads

Noteworthy initial experimental tests of $\vartheta = 3/2$ include direct measurements of the shape of equilibrated crystals of ^{4}He [132] and Pb [133]. As in most measurements of critical phenomena, but even harder here, is the identification of the critical point, in this case the value of x_0 at which rounding begins. Furthermore, as is evident from Eqn (5.36), there are corrections to scaling, so that the "pure" exponent 3/2 is seen only near the edge and a larger effective exponent will be found farther from the edge. For crystals as large as a few mm at temperatures in the range 0.7–1.1 K, ^{4}He $\vartheta = 1.55 \pm 0.06$ was found, agreeing excellently with the Prokrovsky–Talapov exponent. The early measurements near the close-packed (111) facets of Pb crystallites, at least two orders of magnitude smaller, were at least consistent with 3/2, stated conservatively as $\vartheta = 1.60 \pm 0.15$ after extensive analysis. Sáenz and García [134] proposed that in Eqn (5.31) there can be a quadratic term, say $f_2 p^2$ (but neglect the possibility of a quartic term). Carrying out the Legendre transformation then yields an expression with both $x - B$ and $(x - B + f_2^2/3g)^{3/2}$ terms, which they claim will lead to effective values of ϑ between 3/2 and 2. This approach provided a competing model for experimentalists to consider but in the end seems to have produced little fruit.

   As seen in Figure 5.18, STM allows detailed measurement of micron-size crystal height contours and profiles at fixed azimuthal angles. By using STM to locate the initial step down from the facet, first done by Surnev et al. [135] for supported Pb crystallites, x_0 can be located independently and precisely. However, from the 1984 Heyraud–Métois experiment [133] it took almost two decades until the Bonzel group could fully confirm the $\vartheta = 3/2$ behavior for the smooth edges of Pb(111) in a painstaking study [137]. There were a number of noteworthy challenges. While the close-packed 2D network of spheres has six-fold symmetry, the top layer of a (111) facet of an fcc crystal (or of an (0001) facet
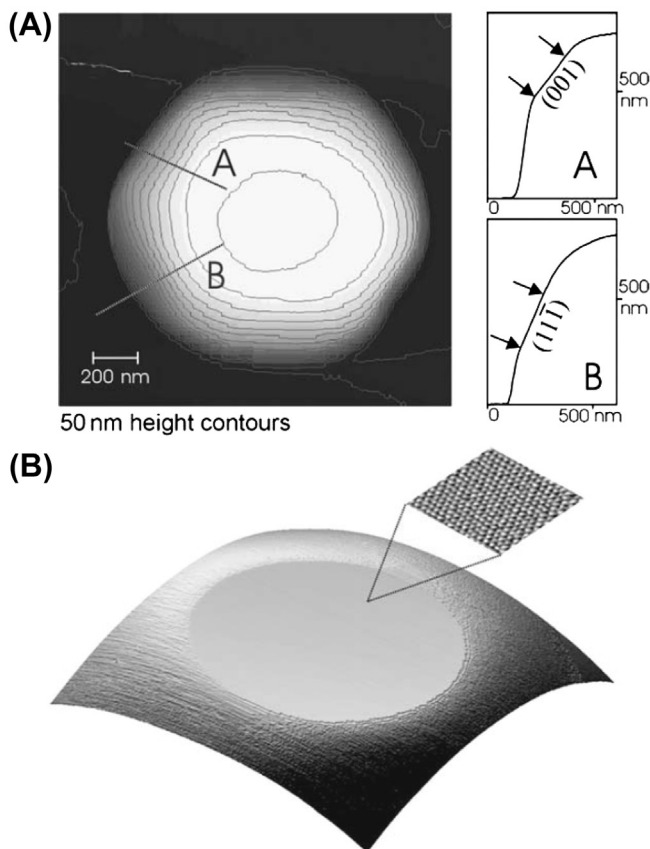
FIGURE 5.18 (A) Micron-size lead crystal (supported on Ru) imaged with a variable-temperature scanning tunneling microscopy at $T = 95$ °C. Annealing at $T = 95$ °C for 20 h allowed it to obtain its stable, regular shape. Lines marked A and B indicate location of profiles. Profile A crosses a (0 0 1)-side facet, while profile B a (1 1 1)-side facet. (B) 770 × 770 nm section of the top part of a Pb crystal. The insert shows a 5.3 × 5.3 nm area of the top facet, confirming its (1 1 $\bar{1}$)-orientation. Both the main image and the insert were obtained at $T = 110$ °C. *From Ref. [141].*

of an hcp crystal) has only three-fold symmetry due to the symmetry-breaking role of the second layer. There are two dense straight step edges, called A and B, with {100} and {111} microfacets, respectively. In contrast to noble metals, for Pb there is a sizable (of order 10%) difference between their energies. Even more significant—when a large range of polar angles is used in the fitting—is the presence of small (compared to {111}) {112} facets for equilibration below 325 K. Due to the high atomic mobility of Pb that can lead to the formation of surface irregularities, Bonzel's group [135] worked close to room temperature. One then finds strong (three-fold) variation of ϑ with azimuthal angle, with ϑ oscillating between 1.4 and 1.7. With a higher annealing temperature of 383 K, [137] report the azimuthal averaged value $\vartheta = 1.487$ (but still with sizable oscillations of about ±0.1); in a slightly earlier short report [137], they give a value $\vartheta = 1.47$ for annealing at

room temperature. Their attention shifted to deducing the strength of step–step re-pulsions by measuring g [138,139]. In the most recent review of the ECS of Pb [140], the authors rather tersely report that the Prokrovsky–Talapov value of 3/2 for ϑ characterizes the shape near the (111) facet and that imaging at elevated temperature is essential to get this result; most of their article relates to comparison of measured and theoretically calculated strengths of the step–step interactions.

Few other systems have been investigated in such detail. Using scanning electron microscopy (SEM) [142] the researchers considered In, which has a tetragonal structure, near a (111) facet. They analyzed the resulting photographs from two different crystals, viewed along two directions. For polar angles $0° \leq \theta < {\sim}5°$ they find $\vartheta \approx 2$ while for $5° \leq \theta \leq 15°$ determine $\vartheta \approx 1.61$, concluding that in this window $\vartheta = 1.60 \pm 0.10$; the two ranges have notably different values of x_0. This group [143] also studied Si, equilibrated at $900°$ C, near a (111) facet. Many profiles were measured along a high-symmetry $\langle 111 \rangle$ zone of samples with various diameters of the order a few μm, over the range $3° \leq \theta \leq 17°$. The results are consistent with $\vartheta = 3/2$, with an uncertainty estimated at 6%. Finally, [144] studied large (several mm) spherical cuprous selenide (Cu_{2-x} Se) single crystals near a (111) facet. Study in this context of metal chalcogenide superionic conductors began some dozen years ago because, other than ^4He, they are the only materials having sub-cm size crystals with an ECS form that can be grown on a practical time scale (viz. over several days) because their high ionic and electronic conductivity enable fast bulk atomic trans-port. For $14.0° \leq \theta \leq 17.1°$ [144] find $\vartheta = 1.499 \pm 0.003$. (They also report that farther from the facet $\vartheta \approx 2.5$, consistent with the Andreev mean field scenario.)

5.6.3 Summary of Highlights of Novel Approach to Behavior Near Smooth Edges

Digressing somewhat, we note that Ferrari, Prähofer, and Spohn [145] found novel static scaling behavior of the equilibrium fluctuations of an atomic ledge bordering a crys-talline facet surrounded by rough regions of the ECS in their examination of a 3D Ising corner (Figure 5.19). This boundary edge might be viewed as a "shoreline" since it is the edge of an islandlike region—the crystal facet—surrounded by a "sea" of steps [146].

Spohn and coworkers assume that there are no interactions between steps other than entropic, and accordingly the step configurations can be mapped to the worldlines of free spinless fermions, as in treatments of vicinal surfaces [37]. However, there is a key new feature that the step number operator is weighted by the step number, along with a Lagrange multiplier λ^{-1} associated with volume conservation of the crystallite. The asymmetry of this term leads to the novel behavior found by the researchers. They then derive an exact result for the step density and find that, near the shoreline:

$$\lim_{\lambda \to \infty} \lambda^{1/3} \rho_\lambda \left(\lambda^{1/3} x \right) = -x(\mathrm{Ai}(x))^2 + (\mathrm{Ai}'(x))^2, \tag{5.34}$$

where ρ_λ is the step density (for the particular value of λ).
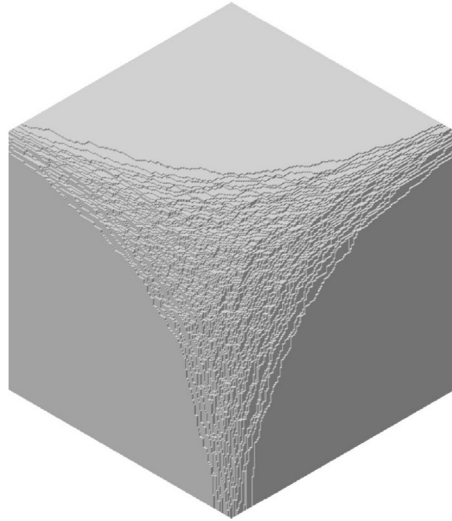
FIGURE 5.19 Simple-cubic crystal corner viewed from the {111} direction. *From Ref. [145].*

The presence of the Airy function Ai results from the asymmetric potential implicit in $\mathcal{H}_F$ and preordains exponents involving 1/3. The variance of the wandering of the shoreline, the top fermionic worldline in Figure 5.20 and denoted by b, is given by

$$\text{Var}\left[b_\lambda(t) - b_\lambda(0)\right] \cong \lambda^{2/3}g\left(\lambda^{-2/3}t\right) \tag{5.35}$$

where t is the fermionic "time" along the step; $g(s) \sim 2|s|$ for small s (diffusive meandering) and $\sim 1.6264 - 2/s^2$ for large s. 1.202… is Apery's constant and N is the number of atoms in the crystal. They find:

$$\text{Var}\left[b_\ell(\ell\tau + x) - b_\ell(\ell\tau)\right] \cong (\mathcal{A}\ell)^{2/3}g\left(\mathcal{A}^{1/3}\ell^{-2/3}x\right), \tag{5.36}$$

where $\mathcal{A} = (1/2)b''_\infty$. This leads to their central result that the width $w \sim \ell^{1/3}$, in contrast to the $\ell^{1/2}$ scaling of an isolated step or the boundary of a single-layer island and to the $\ln \ell$ scaling of a step on a vicinal surface, i.e., in a step train. Furthermore, the
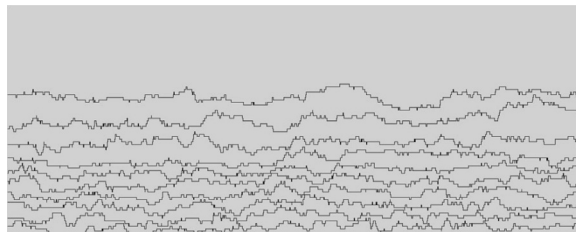

FIGURE 5.20 Snapshot of computed configurations of the top steps (those near a facet at the flattened side portion of a cylinder) for a terrace-step-kink (TSK) model with volume constraint. *From Ref. [145].*

fluctuations are non-Gaussian. The authors also show that near the shoreline, the deviation of the equilibrium crystal shape from the facet plane takes on the Pokrovsky–Talapov [101,104] form with $\vartheta = 3/2$.

From this seminal work, we could derive the dynamic exponents associated with this novel scaling and measure them with STM, as reviewed in Ref. [150].

5.7 Sharp Edges and First-Order Transitions— Examples and Issues

5.7.1 Sharp Edges Induced by Facet Reconstruction

Si near the (111) plane offers an easily understood entry into sharp edges [68,69]. As Si is cooled from high temperatures, the (111) plane in the "(1 × 1)" phase reconstructs into a (7 × 7) pattern [150] around 850 °C, to be denoted T_7 to distinguish it clearly from the other subscripted temperatures. (The notation "(1 × 1)" is intended to convey the idea that this phase differs considerably from a perfect (111) cleavage plane but has no superlattice periodicity.) For comparison, the melting temperature of Si is ∼1420 °C, and the T_R is estimated to be somewhat higher. As shown in Figure 5.21, above T_7, surfaces of
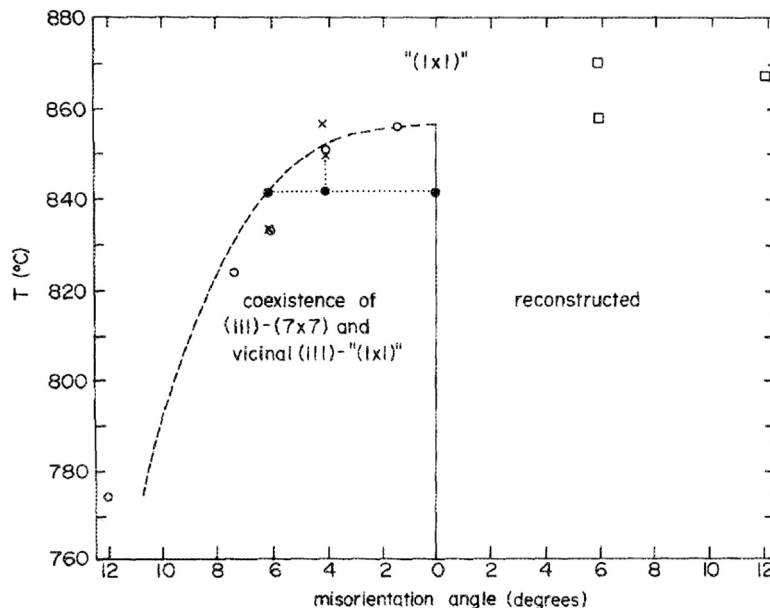
FIGURE 5.21 Summary of experimental results for vicinal Si (111) surface: ○ denotes the temperature at which faceting begins for surfaces misoriented toward the (110) direction, × the faceting temperatures for surfaces misoriented toward the [11$\bar{2}$], and □ the temperatures at which the step structure of surfaces misoriented toward the [$\bar{1}$12] direction change. The dashed line displays a fit of the [$\bar{1}$10] data to Eqn (5.43). The dotted lines show how a four sample phase separates into the states denoted by ● as it is further cooled. *From Ref. [69].*

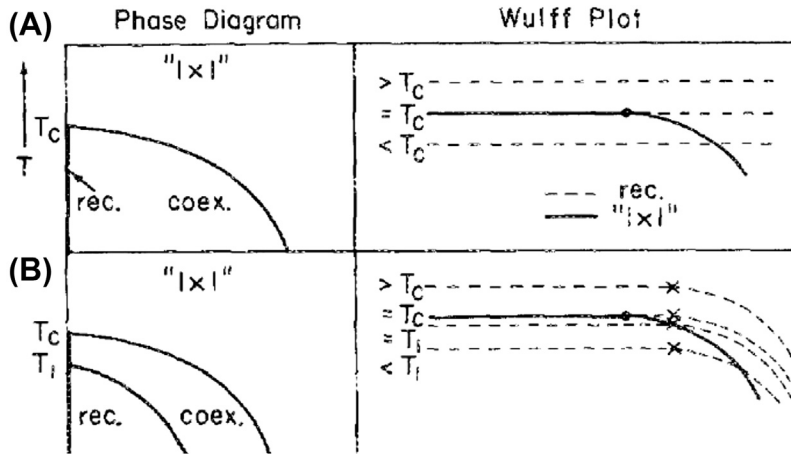**FIGURE 5.22** Wulff plots illustrating the effect of a reconstructive transition on the equilibrium crystal shape (ECS), and corresponding temperature-[mis]orientation phase diagrams. The solid curves represent the ECS with an unreconstructed ["(1 × 1)"] facet, while the dashed curves give the ECS with a reconstructed facet. As temperature decreases, the free energy of the reconstructed facet, relative to that of the unreconstructed facet, decreases. Below the transition temperature T_c (called T_7 in the text), the two shapes intersect, giving a "net" ECS that is the inner envelope of the two. The phase diagram shows regions where all orientations $\tan \theta$ (or $\widehat{m}$) are allowed for the unreconstructed crystal ["(1 × 1)"], regions of phase separation (labeled "coex."), and regions where the reconstruction (labeled "rec.") is allowed for ranges of orientation. The relative size of the reconstructed and unreconstructed facets depends on the free energy to create a step on the reconstructed (111) face, compared to its unreconstructed counterpart: (A) the behavior for extremely large energy to create steps on the (7 × 7) terrace and (A) a smaller such energy. Solid circles mark the sharp edge at the temperature at which the crystal shapes cross. Crosses show the intersection of the facet and the curved part (i.e., the smooth edge) of the crystal shape for the reconstructed phase. *From Ref. [69].*

all orientations are allowed and are unreconstructed. At T_7, a surface in the (111) direction reconstructs but all other orientations are allowed and are unreconstructed. Below T_7, surfaces misoriented toward $[\bar{1}\,\bar{1}2]$ remain stable during cooling (although the step structure changes). On the other hand, on surfaces misoriented toward $[\bar{1}10]$ and $[11\bar{2}]$, the temperature at which the (7 × 7) occurs decreases with increasing misorientation angle $\widehat{m}$. Furthermore, just as the (7 × 7) appears, the surface begins to separate into two phases, one a perfectly oriented (7 × 7) plane $\widehat{m} = 0$ and the second an unreconstructed phase with a misorientation greater than that at higher temperature. As the temperature further decreases, the misorientation of the unreconstructed phase increases. Figure 5.21 depicts this scenario with solid circles and dotted lines for a 4° misoriented sample at 840 °C. This behavior translates into the formation of a sharp edge on the ECS between a flat (7 × 7) line and a rounded "(1 × 1)" curve.

To explain this behavior, one coplots the ECS for the two phases, as in Figure 5.22 [69]. The free energy to create a step is greater in the (7 × 7) than in the "(1 × 1)" phase. In the top panels (A), the step energy for the (7 × 7) is taken as infinite, i.e., much larger than that of the "(1 × 1)" phase, so its ECS never rounds. At T_7 (T_c in the figure), the free energies per area f_0 of the two facets are equal, call them f_7 and f_1, with associated

energies u_7 and u_1 and entropies s_7 and s_1 for the (7×7) and "(1×1)" phases, respectively, near T_7. Then $T_7 = (u_1 - u_7)/(s_1 - s_7)$ and, assuming the internal energies and entropies are insensitive to temperature:

$$f_1 - f_7 = (T_7 - T)(s_1 - s_7). \tag{5.37}$$

Since $s_1 > s_7$ because the (7×7) phase is so highly ordered, we find that $f_1 - f_7 > 0$ below T_7, as illustrated in Figure 5.22. Making connection to thermodynamics, we identify

$$\frac{L}{T_7} = (s_1 - s_7)_{T_7} = \left(\frac{\partial f_7}{\partial T}\right)_{T_7} - \left(\frac{\partial f_1}{\partial T}\right)_{T_7} \tag{5.38}$$

where L is the latent heat of the first-order reconstruction transition.

Corresponding to the minimum of a free energy as discussed earlier, the ECS of the system will be the inner envelope of the dashed and solid traces: a flat (7×7) facet along the dashed line out to the point of intersection, the sharp edge, beyond which it is "(1×1)" with continuously varying orientation. If one tries to construct a surface with a smaller misorientation, it will phase separate into flat (7×7) regions and vicinal unreconstructed regions with the orientation at the curved (rough) side of the sharp edge. Cf. Figure 5.23.

Using the leading term in Eqn (5.35) or (5.36), we can estimate the slope of the coexisting vicinal region and its dependence on temperature[4]: First we locate the sharp edge (recognizing f_0 as f_1 and z_0 as z_1) by noting

$$z_7 = z_1 - 2(\lambda/g)^{1/2}(x - x_0)^{3/2}$$
$$(T_7 - T)\Delta s \approx (f_1 - f_7)_T = \lambda^{3/2} g^{-1/2}(x - x_0)^{3/2} \tag{5.39}$$

Since the slope m there is $-3\lambda(\lambda/g)^{1/2}(x - x_0)^{1/2}$, the temperature dependence of the slope is

$$m = -3\left(\frac{L}{2g}\right)^{1/3}\left(1 - \frac{T}{T_7}\right)^{1/3} \tag{5.40}$$

If the step free energy of the reconstructed phase were only modestly greater than that of the "(1×1)", then, as shown in the second panel in Figure 5.22, the previous high-T behavior obtains only down to the temperature T_1 at which the "(1×1)" curve intersects the (7×7) curve at its [smooth] edge. For $T < T_1$ the sharp edge associated with the interior of the curves is between a misoriented "(1×1)" phase and a differently misoriented (7×7) phase, so that it is these two which coexist. All orientations with smaller misorientation angles than this (7×7) plane are also allowed, so that the forbidden or coexistence regime has the depicted slivered crescent shape. Some other, but physically improbable, scenarios are also discussed by Bartelt et al. [69]. Phaneuf and Williams [68] show (their Figure 3) the LEED-beam splitting for a surface misoriented by $6.4°$ is $\propto (T_7 - T)^{1/3}$ once the surface is cooled below the temperature (which is $<T_7$) when this orientation becomes unstable to phase separation; however, by changing the

---

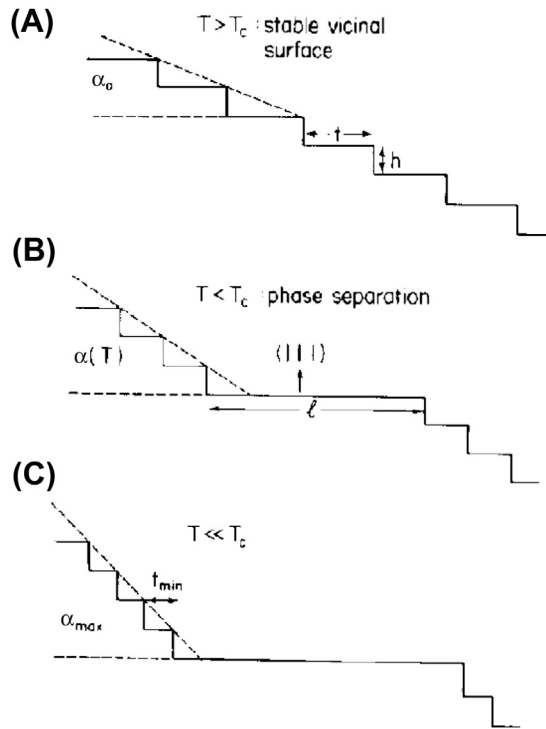[4]There are some minor differences in prefactors from Ref. [69].

FIGURE 5.23 Microscopic view of what happens to a misoriented surface in Figure 5.22 as temperature decreases. (A) At high temperature, the Si(lll) vicinal surface is a single, uniform phase. Initial terrace widths t are typically a few nm, as determined by the net angle of miscut α_0 (i.e., θ_0), and the step-height h, which is one interplanar spacing (~0.31 nm). (B) Below the (7×7) reconstruction temperature (~850 °C), the steps cluster to form a new surface of misorientation angle $a(T)$ (i.e., θ). A facet of (111) orientation with (7×7) reconstruction forms simultaneously. The width of the (111) facet, ℓ, is larger than the experimentally resolvable width of 500 Å. (C) Well below the transition, the step separation reaches a minimum distance, t_{min} ~ 1 nm. No further narrowing occurs, perhaps because surface diffusion is too slow $T \leq 600$ °C. From Ref. [3].

range of fitting, they could also obtain agreement with $(T_7 - T)^{1/2}$, i.e., $\vartheta = 2$. With high-resolution LEED, [151] conclude that the exponent $\bar{\beta} \equiv (\vartheta - 1)/\vartheta = 0.33 \pm 0.05$ (i.e., that $\vartheta = 3/2$. The result does depend somewhat on what thermal range is used in the fit, but they can decisively rule out the mean-field value $\vartheta = 2$. Williams et al. [152] give a more general discussion of vicinal Si, with treatment of azimuthal in addition to polar misorientations. In contrast, synchrotron X-ray scattering experiments by Noh et al. [153,154] report the much larger $\vartheta = 2.3^{+0.8}_{-0.3}$. However, subsequent synchrotron X-ray scattering experiments by [155] obtain a decent fit of data with $\vartheta = 3/2$ and a best fit with $\vartheta = 1.75$ (i.e., $\bar{\beta} = 0.43 \pm 0.07$). (They also report that above 1159 K, the surface exists as a single, logarithmically rough phase.) The origin of the curious value of ϑ in the Noh et al. experiments is not clear. It would be possible to attribute the behavior to impurities, but there is no evidence to support this excuse, and indeed for the analogous behavior near the reconstructing (331) facet of Si (but perhaps a different sample), Noh

et al. [156] found $\vartheta = 1.47 \pm 0.1$. It is worth noting that extracting information from X-ray scattering from vicinal surfaces requires great sophistication (cf. the extensive discussion in Ref. [157]) and attention to the size of the coherence length relative to the size of the scattering region [158], as for other diffraction experiments.

Similar effects to reconstruction (viz. the change in f_0) could be caused by adsorption of impurities on the facet [159]. Some examples are given in a review by Somorjai and Van Hove [160]. In small crystals of dilute Pb-Bi-Ni alloys, cosegregation of Bi-Ni to the surface has a similar effect of reversibly changing the crystal structure to form {112} and {110} facets [161]. There is no attempt to scrutinize the ECS to extract an estimate of ϑ. Meltzman et al. [162] considered the ECS of Ni on a sapphire support, noting that, unlike most fcc crystals, it exhibits a faceted shape even with few or no impurities, viz. with {111}, {100}, and {110} facets; {135} and {138} emerged at low oxygen pressure and additionally {012} and {013} at higher pressure.

The phase diagram of Pt(001), shown in Figure 5.24 and studied [163] using synchrotron X-ray scattering, at first seems similar to that of Si near (111) [223,224,225], albeit with more intricate magic phases with azimuthal rotations at lower temperatures, stabilized by near commensurability of the period of their reconstruction and the separation of their constituent steps. In the temperature-misorientation (surface slope) phase diagram, shown in Figure 5.24, the (001) facet undergoes a hexagonal reconstruction at $T_6 = 1820$ K (well below the bulk melting temperature of 2045 K). For samples misoriented from the (100) direction (which are stable at high temperature), there is coexistence between flat reconstructed Pt(001) and a rough phase more highly
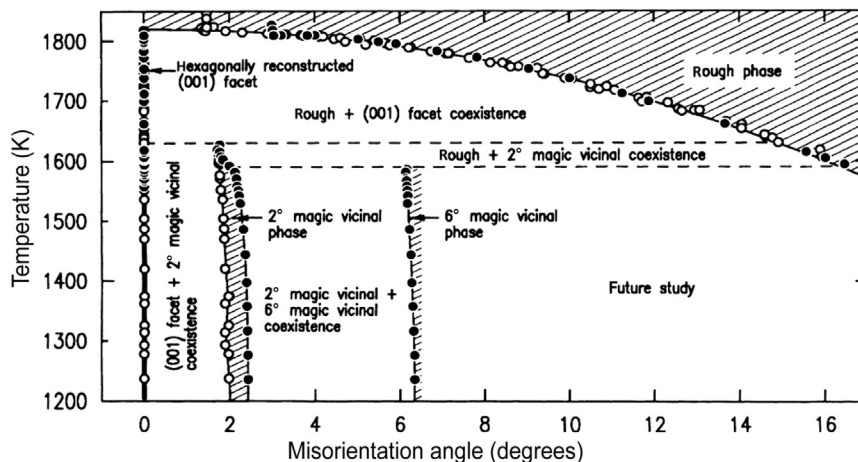
FIGURE 5.24 Orientational phase diagram of vicinal Pt (001) misoriented toward the [110] direction. Single-phase regions are hatched, and two-phase coexistence regions are unhatched. Solid lines are boundaries between two phases. Dashed lines mark triple points. Open circles show misorientation angles measured for a sample miscut by 1.4° toward the [110] direction, while solid circles show tilt angles measured for a sample miscut by 3.0°. *From Ref. [163].*

misoriented than it was at high temperature, with a misorientation that increases as temperature decreases. However, they find $\bar{\beta} = 0.49 \pm 0.05$, or $\vartheta = 1.96$, consistent with mean field and inconsistent with $\bar{\beta} = 1/3$ or $\vartheta = 3/2$ of Prokrovsky–Talapov. The source of this mean-field exponent is that in this case the (001) orientation is rough above T_6. Hence, in Eqn (5.31) B vanishes, leaving the expansion appropriate to rough orientations. Proceeding as before, Eqn (5.35) becomes

$$f_p(p) = f_0 + Dp^2 \Rightarrow \tilde{f}(\eta) = f_0 - \eta^2 \Big/ 4D, \tag{5.41}$$

where the result for $\tilde{f}(\eta)$ is reached by proceeding as before to reach the modification of Eqn (5.35). Thus, there is no smooth edge take-off point (no shoreline) in the equivalent of Figure 5.22, and one finds the reported exponent ϑ near 2.

The effect of reactive and nonreactive gases metal catalysts has long been of interest [211]. Various groups investigated adsorbate-induced faceting. Walko and Robinson [164] considered the oxygen-induced faceting of Cu(115) into O/Cu(104) facets, using Wulff constructions to explain their observations. The researchers found three temperature regimes with qualitatively different faceting processes. Szczepkowicz et al. [165] studied the formation of {211} facets by depositing oxygen and paladium on tungsten, both on (111) facets and on soherical crystals. While the shape of the facets is different for flat and curved surfaces, the distance between parallel facet edges is comparable, although the area of a typical facet on a curved surface is an order of magnitude greater. There is considerable information about facet sizes, width of the facet-size distribution, and surface rms roughness.

For 2D structures on surfaces, edge decoration can change the shape of the islands. A well-documented example is Pt on Pt(111). As little as 10^{-3} ml of CO produces a 60° rotation of the triangular islands by changing the balance of the edge free energies of the two different kinds of steps forming the island periphery [166]. Stasevich et al. [167] showed how decoration of single-layer Ag islands on Ag(111) by a single-strand "necklace" of C_{60} dramatically changes the shape from hexagonal to circular. With lattice-gas modeling combined with STM measurements, they could estimate the strength of C_{60}-Ag and C_{60}-C_{60} attractions. Generalizations to decoration on systems with other symmetries is also discussed [167].

5.8 Gold–Prototype or Anomaly of Attractive Step–Step Interaction?

Much as ^{4}He and Pb are the prototypical materials with smooth edges, Au is perhaps the prime example of a surface with sharp edges, around (1111) and (100) facets (cf. e.g., Ref. [1]). Care must be taken to ensure that the surface is not contaminated by atoms (typically C) from the supporting substrate [168]. (See similar comments by Handwerker et al. [169] for ceramics, which have a rich set of ECS possibilities.) To describe these systems phenomenologically, the projected free energy expansion in Eqn (5.1) requires a negative term to generate a region with negative curvature, as in Figure 5.7, so that the

two orientations joined by the Maxwell double-tangent construction correspond to the two sides of the sharp edge. Thus, for sharp edges around facets, the more-left minimum must be in the high-symmetry facet direction.

In a mean field-based approach, Wang and Wynblatt [168] included a negative quadratic term, with questionable physical basis. Emundts et al. [170] instead took the step–step interaction to be attractive ($g < 0$) in Eqn (5.1). Then, proceeding as above, they find

$$x_0 = \frac{1}{\lambda}\left[B - \frac{4}{27}|g|\left(\frac{g}{c}\right)^2\right], \quad p_c = \frac{2|g|}{3c},$$ (5.42)

where p_c is the tangent of the facet contact angle. Note that both the shift in the facet edge from B and the contact slope increase with $|g|/c$. Emundts et al. [170] obtain estimates of the key energy parameters in the expansion for the sharp edges of both the (111) and (100) facets. They also investigate whether it is the lowering of the facet free energy f_0 that brings about the sharp edges, in the manner of the case of Si(111) discussed above. After reporting the presence of standard step–step repulsions (leading to narrowing of the TWD) in experiments on flame-annealed gold, Shimoni et al. [171] then attribute to some effective long-range attraction—with undetermined dependence on ℓ—the (nonequilibrium) movement of single steps toward step bunches whose steps are oriented along the high-symmetry $\langle 110 \rangle$.

Is it possible to find a generic long-range attractive $A\ell^{-2}$ step–step interaction ($A < 0$) for metals and elemental semiconductors (where there is no electrostatic attraction between oppositely charged atoms)? Several theoretical attempts have only been able to find such attractions when there is significant alternation between "even" and "odd" layered steps. Redfield and Zangwill consider whether surface relaxation can produce such an attraction, pointing out a flaw in an earlier analysis assuming a rigid relaxation by noting that for large step separations, the relaxation must return to its value for the terrace orientation. Since atomic displacements fall off inversely with distance from a step, the contribution to the step interaction can at most go like ℓ^{-2} and tend to mitigate the combined entropic and elastic repulsion. They argue that this nonlinear effect is likely to be small, at least for metals. It is conceivable that on an elastically highly anisotropic surface, the elastic interaction might not be repulsive in special directions, although I am not aware of any concrete examples.

By observing that the elastic field mediating the interaction between steps is that of a dipole applied on a stepped rather than on a flat surface, Kukta et al. [172] deduce a correction to the ℓ^{-2} behavior of the Marchenko–Parshin [41] formula that scales as $\ell^{-3}\ln\ell$. Using what was then a state-of-the-art semiempirical potential, the embedded atom method (EAM) [228], the authors find that this can lead to attractive interactions at intermediate values of ℓ. However, their "roughness correction" term exists only when the two steps have unlike orientations (i.e., one up and one down, such as on opposite ends of a monolayer island or pit). For the like-oriented steps of a vicinal surface or near a facet edge, the correction term vanishes. The oft-cited paper then invokes three-step

interactions, which are said to have the same size as the correction term, as a way to achieve attractive interactions. Although the authors discuss how this idea relates to the interaction between an isolated step and a step bunch, they do not provide the explicit form of the threefold interaction; their promise that it will be "presented elsewhere" has not, to the best of my searching, ever been fulfilled. Prévot and Croset [173] revisited elastic interactions between steps on vicinals and found that with a buried-dipole model (rather than the surface-dipole picture of Marchenko and Parshin), they could achieve "remarkable agreement" with molecular dynamics simulations for vicinals to Cu and Pt (001) and (111), for which data is fit by $E_2^{MD}\ell^{-2} + E_3^{MD}\ell^{-3}$. The tabulated values of E_2^{MD} indeed agree well with their computed results for their improved elastic model, which includes the strong dependence of the interaction energy on the force direction. While there is barely any discussion of E_3, plots of the interaction are always repulsive. Hecquet [174] finds that surface stress modifies the step–step interaction compared to the Marchenko–Parshin result, enhancing the prefactor of ℓ^{-2} nearly threefold for Au(001); again, there is no mention of attractive interactions over any range of step separations.

In pursuit of a strictly attractive ℓ^{-2} step interaction to explain the results of Shimoni et al. [171], Wang et al. [175] developed a model based on the SSH model [176] of polyacetylene (the original model extended to include electron–electron interaction), focusing on the dimerized atom rows of the (2×1) reconstruction of Si(001). The model produces an attractive correction term to the formula derived by Alerhand et al. [177] for interactions between steps on Si(001), where there is ABAB alternation of $(2 \times 1$ and $1 \times 2)$ reconstructions on neighboring terraces joined at single-height steps. For this type of surface, the correction has little significance, being dwarfed by the logarithmic repulsion. It also does not occur for vicinals to high-symmetry facets of metals. However, for surfaces such as Au(110) with its missing row morphology [178] or adsorbed systems with atomic rows, the row can undergo a Peierls [179] distortion that leads to an analogous dimerization and an ℓ^{-2} attraction. There have been no tests of these unsung predictions by electronic structure computation.

Returning to gold, applications of the glue potential (a semiempirical potential rather similar to EAM), Ercolessi et al. [180] were able to account for reconstructions of various gold facets, supporting that the sharp edges on the ECS are due to the model used for Si(111) rather than attractive step interactions. Studies by this group found no real evidence for attractive step interactions [181].

In an authoritative review a decade ago, Bonzel [2]— the expert in the field who has devoted the most sustained interest in ECS experiments on elemental systems— concluded that it was not possible to decide whether the surface reconstruction model or attractive interactions was more likely to prove correct. In my view, mindful of Ockham's razor, the former seems far more plausible, particularly if the assumed attractive interaction has the ℓ^{-2} form.

The phase diagram of surfaces vicinal to Si(113) presents an intriguing variant of that vicinal to Si(111). There is again a coexistence regime between the (113) orientation and progressively more highly misoriented vicinals as temperature is reduced below a

threshold temperature T_t, associated with a first-order transition. However, for higher temperatures $T > T_t$ there is a continuous transition, in contrast to the behavior on (111) surfaces for $T > T_7$. Thus, Song and Mochrie [182] identify the point along (113) at which coexistence vanishes, i.e., T_t, as a tricritical point, the first such point seen in a misorientation phase diagram. To explain this behavior, Song and Mochrie invoke a mean-field Landau theory argument in which the cubic term in p is proportional to $(T - T_t)$, so negative for $T < T_t$, with a positive quartic term. Of course, this produces the observed generic behavior, but the exponent $\bar{\beta}$ is measured as 0.42 ± 0.10 rather than the mean-field value 1. Furthermore, the shape of the phase diagram differs from the mean-field prediction and the amplitude of the surface stiffness below T_t is larger than above it, the opposite of what happens in mean field. Thus, it is not clear in detail what the interactions actually are, let alone how an attractive interaction might arise physically.

5.9 Well-Established Attractive Step–Step Interactions Other Than ℓ^{-2}

For neutral crystals, there are two ways to easily obtain interactions that are attractive for some values of ℓ. In neither case are the interactions monotonic long range. The first is short-range local effects due to chemical properties of proximate steps, while the other is the indirect Friedel-like interaction.

5.9.1   Atomic-Range Attractions

At very small step separations, the long-range ℓ^{-2} monotonic behavior is expected to break down and depend strongly on the local geometry and chemistry. Interactions between atoms near step edges are typically direct, thus stronger than interactions mediated by substrate elastic fields or indirect electronic effects (see below). We saw earlier that a ℓ^{-3} higher order term arises at intermediate separations [42], and further such terms should also appear with decreasing ℓ. On TaC(910) [vicinal to (001) and miscut toward the [010] direction], Zuo et al. [183] explained step bunching using a weak $\ell^{-3[\pm 0.5]}$ attraction in addition to the ℓ^{-2} repulsion. (The double-height steps are electrically neutral.) Density-functional theory (DFT) studies were subsequently performed for this system by Shenoy and Ciobanu [184]. Similarly, Yamamoto et al. [185] used an attractive ℓ^{-3} dipole-quadrupole interaction to explain anomalous decay of multilayer holes on $SrTiO_3(001)$.

More interesting than such generic effects are attractions that occur at very short step separations for special situations. A good example is Ciobanu et al. [186], who find an attraction at the shortest separation due to the cancellation of force monopoles of two adjacent steps on vicinal Si(113) at that value of ℓ.

As alluded to above, most of our understanding of the role of ℓ^{-2} step interactions comes from the mapping of classical step configurations in 2D to the worldlines of spinless fermions in 1D. Unlike fermions, however, steps can touch (thereby forming double-height steps), just not cross. Such behavior is even more likely for vicinal fcc or

bcc (001) surfaces, where the shortest possible "terrace," some fraction of a lateral nearest-neighbor spacing, amounts to touching fermions when successive layers of the crystal are described with simple-cubic rather than layer-by-layer laterally offset co-ordinates. Sathiyanarayanan et al. [187] investigated some systematics of step touching, adopting a model in which touching steps on a vicinal cost an energy ϵ_t. Note that $\epsilon_t = \infty$ recoups the standard fermion model. For simplicity, the short study concentrates on the "free-fermion" case $\tilde{A} = 0$, i.e., $\varrho = 2$ (cf. Eqn (5.28)). Even for $\epsilon_t = 0$, there is an effective attraction, i.e., $\varrho < 2$, since the possibility of touching broadens the TWD. This broadening is even more pronounced for $\epsilon_t < 0$. In other words, such short-range effects can appear, for a particular system, to contribute a long-range attraction. Closer examination shows that this attraction is a finite-size effect that fades away for large values of $\langle \ell \rangle$. In our limited study, we found that fits of simulated data to the GWD expression could be well described by the following finite-size scaling form, with the indicated three fitting parameters:

$$\varrho_{\text{eff}} = 2 - (0.9 \pm 0.1)\langle \ell \rangle^{-0.29 \pm 0.07} \exp\left[- (3.3 \pm 0.2)\epsilon_t \big/ k_B T \right]. \tag{5.43}$$

While Eqn (5.43) suggests that making the step touching more attractive (decreasing ϵ_t) could decrease β_{eff} without limit, instabilities begin to develop, as expected since Lässig [188] showed that for $\tilde{A} < -1/4$, i.e., $A < -(k_B T)^2/4\tilde{\beta}$, a vicinal surface becomes unstable (to collapse to step bunches). Correspondingly, the lowest value tabulated in Sathiyanarayanan et al. [187] is $\epsilon_t/k_B T = -0.2$.

To distinguish true long-range (ℓ^{-2}) attractions on vicinal surfaces requires measurements of several different vicinalities (i.e., values of $\langle \ell \rangle$). Likewise, in analyses of ECS data, consideration of crystallites of different sizes would seem necessary. Wortis [1] noted the importance of size dependence in other contexts.

Along this theme, an instructive specific case is the "sticky-step" or, more formally, the p-RSOS (restricted solid-on-solid with point-contact attractions between steps) model explored in detail by Akutsu [189] using the product wavefunction renormalization group (PWFRG) method, calculating essentially the ECS (see Figure 5.25) and related properties. Steps are zig-zag rather than straight as in the preceding Sathiyanarayanan model, so her "stickiness" parameter ϵ_{int} is similar but not identical to ϵ_t. She finds that in some temperature regimes, nonuniversal non-Prokrovsky–Talapov values of ϑ occur. Specifically, let $T_{f,111}(\epsilon_{int}/\epsilon,\phi_0)$ and $T_{f,001}(\epsilon_{int}/\epsilon,\phi_0)$ be the highest temperature at which a first-order phase transition (sharp edge) occurs for the (111) and (001) facets, respectively, where ϕ_0 indicates the position along the ECS. Note $T_{f,111}(\epsilon_t/\epsilon,\phi_0) = (0.3610 \pm 0.0005)\epsilon/k_B > T_{f,111}(\epsilon_{int}/\epsilon,\phi_0) = (0.3585 \pm 0.0007)\epsilon/k_B$. For $k_B T/\epsilon = 0.37$, so $T > T_{f,111}(-0.5,\pi/4)$, Akutsu recovers Prokrovsky–Talapov values for ϑ and ϑ_t, but for $k_B T/\epsilon = 0.36$ (shown in Figure 5.26), so $T_{f,111}(-0.5,\pi/4) > T > T_{f,001}(-0.5,\pi/4)$, the values are very different: $\vartheta = 1.98 \pm 0.03$ and $\vartheta_t = 3.96 \pm 0.08$, more like mean field. For $\phi_0 = 0$ (tilting toward the $\langle 100 \rangle$ direction), only standard Prokrovsky–Talapov exponents are found. Upon closer examination with Monte Carlo simulations, Akutsu finds large step bunches for $T < T_{f,100}$ but step droplets for $T_{f,001} < T < T_{f,111}$. The details are beyond the
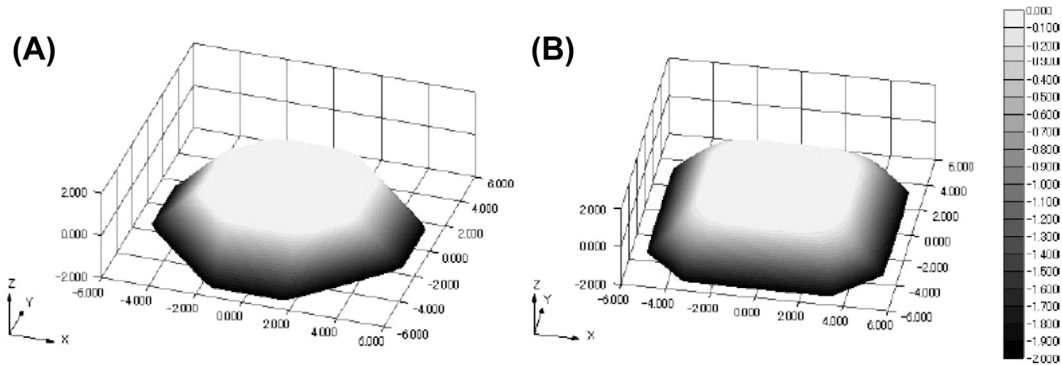
FIGURE 5.25 Perspective views of essentially the equilibrium crystal shape (actually the Andreev surface free energy divided by $k_B T$) around the (001) facet calculated by the transfer-matrix method with the product-wave-function renormalization group algorithm at $k_B T/\epsilon_1 = 0.3$. (A) Restricted solid-on-solid with point-contact attractions between steps (p-RSOS) model ($\epsilon_{int}/\epsilon_1 = -0.5$). (B) For comparison, the original unsticky RSOS model ($\epsilon_{int} = 0$). *From Ref. [189].*
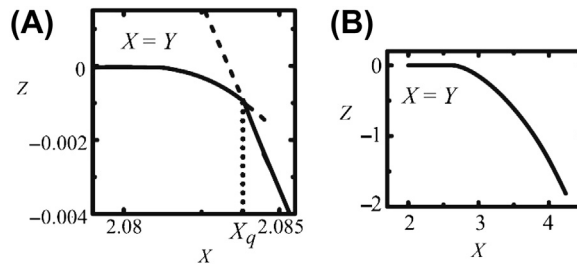

FIGURE 5.26 Profiles in the diagonal direction of the surface in Figure 5.25, still at $k_B T/\epsilon_1 = 0.3$. Broken lines represent metastable lines. (A) $k_B T/\epsilon_1 = 0.36$, $\epsilon_{int}/\epsilon_1 = -0.5$, on a very fine length scale. The edge of the (111) facet is denoted by X_q. (B) The original RSOS model ($\epsilon_{int} = 0$) on a much coarser scale. On this scale (and on an intermediate scale not included here), the profiles are flat until the edge. On the intermediate scale, the region beyond X_q is starts deviating rather smoothly for $k_B T/\epsilon_1 = 0.35$ but looks straight for $k_B T/\epsilon_1 = 0.36$ and 0.37. See text and source. *From Ref. [189].*

scope of this review, but eventually Akutsu deduces an expansion of the projected free energy that includes either a quadratic term or a term after the linear term that has the form $|p|^\zeta$, with $\zeta > 1$.

5.9.2 Attractions at Periodic Ranges of Separation via Oscillatory Friedel-Type Interactions

Oscillatory (in sign) interactions, mediated by substrate conduction electrons, between steps ipso facto lead to attractive interactions between steps. As reviewed by Einstein [94], such interactions have been known for many decades to account for the ordered patterns of adsorbates on metal surfaces [190]. While at short range, all electrons

contribute, asymptotically the interaction is dominated by the electron(s) at the Fermi surface or, from another perspective, the nonanalyticity in the response function at the nesting vector. The interaction energy has the form

$$E_{\text{pair}}^{\text{asymp}} \propto \ell^{-n} \cos\left(2k_F\ell + \Phi\right) \tag{5.47}$$

This, or its analogue for interacting local magnetic species, is called the RKKY [191,192] interaction. (The community studying magnetism now labels as RKKY any interaction mediated by substrate electrons, not just the asymptotic limit written down in the RKKY papers.) The phase factor Φ is the nonperturbative result is the scattering phase shifts at the two atoms that are interacting; it is absent in the perturbational approach to this problem used in the RKKY papers. The exponent n indicates the decay envelope. For interacting bulk entities, $n = 3$, the standard RKKY results. On metal surfaces, the leading term in the propagator is canceled by the image charge, leading to $n = 5$, with very rapid decay [94,190]. Such effects are insignificant for adatom interactions but can be more potent when a whole step participates. Redfield and Zangwill [193] show that a line of localized perturbations will generate an interaction with n reduced by subtracting 1/2 and Φ augmented by $\pi/4$. They used this result, with $n = 9/2$, to account for Frohn et al.'s [194] remarkable experimental results on vicinal Cu(001): from their observed bimodal TWD, Frohn et al. deduced that the step–step interaction is attractive for intermediate distances three to five atoms. Indeed, it was their striking observation that led to several of the previously discussed theory papers that claimed to find long-range step attractions.

When there are metallic surface states (i.e., surface states for which their 2D band dispersion relation crosses the Fermi energy E_F) of Shockley nature (lying in a 2D band gap containing E_F), the indirect interaction has a much slower decay, with $n = 2$ [94,195–199]. Furthermore, the Fermi wavevector typically is much smaller than that of bulk states, so the period of the oscillation in real space is much larger. Perhaps the most familiar metallic surface on metals is that at the center of the surface Brillouin zone ($\overline{\Gamma}$) of the (111) surfaces of noble metals, which exist inside the necks of the Fermi surface, discussed in textbooks, e.g. [200]. This is the state that produces the famous wave structure in Eigler's group's dramatic STM images [201] of atoms on metal surfaces. However, there is a less well-known metallic surface state on Cu(001), discovered relatively late (compared to other surface states) by Kevan [202]; it is centered at the zone-edge center $\overline{X}$ rather than $\overline{\Gamma}$, and may provide a better explanation of the Frohn et al. results in the Redfield–Zangwill framework. For surface-state mediated interactions between steps, their formula indicates $n = 3/2$, comparable to the entropic and elastic repulsions.

The effect of surface-state mediated interactions on TWDs was elucidated by Pai et al. [203] in combined experimental and theoretical examination of vicinal Ag(110), which has a metallic surface state centered at $\overline{Y}$, the middle of the shorter edge of the rectangular surface Brillouin zone [204]. In essence, the surface state introduces a second length scale, the Fermi wavelength λ_F, in addition to $\langle\ell\rangle$, with the major consequence that the TWD is no longer a function of the single scaled dimensionless variable s but depends

also on $\langle \ell \rangle$. With a suitable model potential, Pai et al. [203] could then account for the different TWDs at a few different misorientations (i.e., mean step spacings). Indeed, to establish convincingly that this Friedel-like effect is significant, one must measure several different values of $\langle \ell \rangle$. While this paper has been cited with regard to other modifications of TWDs (cf. e.g., Refs [205,206]), I have found no other investigations of Friedel-like effects on TWDs for several misorientations of the same substance.

Patrone and Einstein [207] discuss other issues related to possible anisotropic surface state dispersion as well as showing the insensitivity to the point in the surface Brillouin zone about which the state is centered.

5.10 Conclusions

An aspect of ECS studies on which there has been substantial progress since the 1980s, but which has received little attention in this chapter, is comparing and reconciling the values of the characteristic energies (surface free energy per area, step free energy per length, and step–step repulsion strength) that are extracted from experimental measurements with ever-improving calculations (using density functional theory) of these energies. Bonzel's review [2], as well as Nowicki and Bonzel [140], Bonzel et al. [139], Barreteau et al. [226], Yu et al. [227], contain extensive coverage of this issue for the soft metals to which his group has devoted exhaustive attention. Williams [59] review most results for silicon. Such efforts to find absolute energies has also taken place in studies of island shapes, e.g., of TiN(001) [208] and (111) [209].

There are several significant advances in generic understanding of ECS since the 1980s. The Prokrovsky–Talapov ($\vartheta = 3/2$) critical phenomena near the edge of the smoothly curved region near a facet has proved to be far more robust and general than originally realized, while novel behavior is predicted in a very special direction. Even though invoked in many accounts of sharp edges, long-range attractive ℓ^{-2} do not have an apparent physical basis, except perhaps in idiosyncratic cases. The likely cause is a reconstruction or adsorption that changes the surface free energy of the facet orientation. On the other hand, hill-and-valley structures are widely seen, and the possibility of azimuthal in addition to polar misorientation can lead to astonishingly rich phase diagrams. Of course, nonequilibrium considerations open up a whole new universe of behavior. Furthermore, at the nanoscale, cluster shape is very sensitive to the particulars of a system, with the addition or removal of a single atom leading to a substantial change in shape, rather like biological systems, in contrast to the macroscale phenomena that have been treated in this chapter.

Acknowledgments

References

[1] Wortis M. Equilibrium crystal shapes and interfacial phase transitions. In: Vanselow R, Howe R, editors. Chemistry and physics of solid surfaces, VII. Berlin: Springer-Verlag; 1988. p. 367–405.

[2] Bonzel HP. Phys Rep 2003;385:1.

[3] Williams ED, Bartelt NC. Ultramicroscopy 1989;31:36.

[4] Rottman C, Wortis M. Phys Rep 1984;103:5979.

[5] Pimpinelli A, Villain J. Physics of crystal growth. Cambridge (England): Cambridge University Press; 1998.

[6] Landau LD, Lifshitz EM. Statistical physics, part 1. revised and enlarged by Lifshitz EM and Pitaevskii LP. 3rd ed. Oxford: Pergamon Press; 1980. pp. 155.

[7] Nozières P. Shape and growth of crystals. In: Godrèche C, editor. Solids far from equilibrium. Cambridge: Cambridge University Press; 1992.

[8] Sekerka RF. Theory of crystal growth morphology. In: Müller G, Métois J-J, Rudolph P, editors. Crystal growth – from fundamentals to technology. Amsterdam: Elsevier; 2004. p. 55.

[9] van Beijeren H, Nolden I. "The roughening transition", structure and dynamics of surfaces II: phenomena, models, and methods. In: Schommers W, von Blanckenhagen P, editors. Topics in current physics, vol. 43. Berlin: Springer; 1987. p. 299.

[10] J. W. Gibbs, "On the equilibrium of heterogeneous substances", Transactions of the Connecticut academy of arts and sciences, 3, 108 248, 343 524, (1874–1878). Reproduced in both the Scientific Papers. 1906; 55–353 and The Collected Works of Gibbs JW. 1928; 55–353. The Collected Works of Gibbs JW, in two volumes, Longley WR, Van Name RG, editors. New Haven: Yale University Press; 1957 (1928).

[11] Herring C. Phys Rev 1951;82:87–93.

[12] Herring C. The use of classical macroscopic concepts in surface energy problems. In: Gomer R, Smith CS, editors. Conference arranged by National Research Council, Lake Geneva, 1952. Chicago: University of Chicago Press; 1953b. p. 5–81 [Chapter 1].

[13] Curie P. Bull Soc Min Fr 1885;8:145.

[14] Wulff G. Z für Kryst Mineral 1901;34:449.

[15] Hilton H. Mathematical crystallography. Oxford; 1903.

[16] Liebmann H. Z Krist 1914;53:171.

[17] von Laue M. Der Wulffsche Satz für die Gleichgewichtsform von Kristallen. Z Krist 1943;105:124.

[18] Dinghas A. Z Krist 1944;105:303–14.

[19] Burton WK, Cabrera N, Frank FC. Phil Trans R Soc A 1951;243:299.

[20] Frank FC. Metal surfaces. Metals Park (OH): American Society for Metals; 1962/3 [Chapter 1]p. 1–15.

[21] Mullins WW. In: Metal surfaces. Metals Park (OH): American Society for Metals; 1962/3. p. 17–62 [Chapter 2].

[22] Jackson KA. In: Ueda R, Mullin JB, editors. Crystal growth and characterization. Amsterdam: North-Holland; 1975. p. 21.

[23] Chernov AA. Sov Phys Uspekhi 1961;4:116.

[24] Cerf R, Picard J. The Wulff crystal in ising and percolation models. Berlin: Springer; 2006.

[25] Dobrushin RL, Kotecký R, Shlosman S. The Wulff construction: a global shape from local interactions. Providence (RI): AMS; 1992. preprint: http://www.cpt.univ-mrs.fr/dobrushin/DKS-book.pdf.

[26] Almgren F, Taylor JE. Fractals 1996;3:713.

[27] Peng D, Osher S, Merriman B, Zhao H-K. The geometry of Wulff crystal shapes and its relation with Riemann problems. In: Nonlinear partial differential equations. Contemp. Math, vol. 238. Providence (RI): AMS; 1999. p. 251–303.

[28] Dobrushin RL, Kotecký R, Shlosman SB. J Stat Phys 1993;12:1.

[29] Dacorogna B, Pfister CE. J Math Pures Appl 1992;71:97–118.

[30] Fonseca I. Proc R Soc Lond A 1991;432:125.

[31] De Coninck J, Dunlop F, Rivasseau V. Commun Math Phys 1989;121:401.

[32] Miracle-Sole S. In: Miracle-Sole S, Ruiz J, Zagrebnov V, editors. Mathematical results in statistical mechanics. Singapore: World Scientific; 1999. p. 83 [arXiv:1206.3736v1].

[33] Miracle-Sole S. Wulff shape of equilibrium crystals. 2013 [arXiv:1307.5180v1].

[34] Pfister CE. Helv Phys Acta 1991;64:953.

[35] Miracle-Sole S, Ruiz J. On the Wulff construction as a problem of equivalence of statistical ensembles. In: Fannes M, Verbeure A, editors. On three levels: micro, meso and macroscopic approaches in physics. New York: Plenum Press; 1994. p. 295–302 [arXiv:1206.3739v1].

[36] Fonseca I, Müller S. Proc R Soc Edinb 1991;119:125.

[37] Jayaprakash C, Rottman C, Saam WF. Phys Rev B 1984;30:6549. in the Hamiltonian in their Eqn 3, the factor t/2 should have been t. See erratum in Ref. [152].

[38] Nelson RC, Einstein TL, Khare SV, Rous PJ. Surf Sci 1993;295:462–84.

[39] Ibach H, Schmickler W. Phys Rev Lett 2003;91:016106.

[40] Stewart J, Pohland O, Gibson JM. Phys Rev B 1994;49:13848.

[41] Marchenko VI, Parshin A Ya. Sov. Phys. JETP 1980;52:129 [Zh Eksp Teor Fiz 1980;79:257.].

[42] Najafabadi R, Srolovitz DJ. Surf Sci 1994;317:221–34.

[43] Duxbury PM, Pence TJ, editors. Dynamics of crystal surfaces and interfaces. New York: Plenum; 1997.

[44] Carlon E, van Beijeren H. Phys Rev E 2000;62:7646.

[45] van Albada SB, Rost MJ, Frenken JWM. Phys Rev B 2002;65:205421.

[46] Bonzel HP, Preuss E. Surf Sci 1995;336:209.

[47] Lieb EH, Wu FY. In: Domb C, Green MS, editors. Phase transitions and critical phenomena, vol. 1. London: Academic Press; 1972. p. 331.

[48] Lieb EH. Phys Rev Lett 1967;19:108.

[49] van Beijeren H. Phys Rev Lett 1977;38:993.

[50] Nolden IM, van Beijeren H. Phys Rev B 1994;49:17224.

[51] Kosterlitz JM, Thouless DJ. J Phys C 1973;6:1181.

[52] Kosterlitz JM. J Phys C 1974;7:1046.

[53] Yang CP. Phys Rev Lett 1967;19:586.

[54] Sutherland B, Yang CN, Yang CP. Phys Rev Lett 1967;19:588.

[55] Callen HB. Thermodynamics and an introduction to the mostatistics. 2nd ed. New York: Wiley; 1985.

[56] Kossel W. Nachr Ges Wiss Göttingen 1927;143.

[57] Kossel W. Ann Phys 1934;21:457–80.

[58] García N, Sáenz JJ, Cabrera N. Physica 1984;124B:251.

[59] Jeong H-C, Williams ED. Surf Sci Rep 1999;34:171.

[60] Cahn JW, Carter WC. Metall Mater Trans A Phys Metall Mater Sci 1996;27:1431–40 [arXiv:cond-mat/0703564v1].

[61] Hoffman DW, Cahn JW. Surf Sci 1972;31:368. Cahn JW, Hoffman DW. Acta Met 1974;22:1205.

[62] Wheeler AA. J Stat Phys 1999;95:1245–80.

[63] Balibar S, Castaing B. J Phys Lett 1980;41:L329.

[64] Keshishev KO, Parshin AY, Babkin AV. Sov Phys JETP 1981;53:362.

[65] Wolf PE, Balibar S, Gallet F. Phys Rev Lett 1983;51:1366.

[66] Wolf PE, Gallet F, Balibar S, Rolley E, Nozières P. J Phys Fr 1985;46:1987.

[67] Balibar S, Alles H, Parshin A Ya. Rev Mod Phys 2005;77:317.

[68] Phaneuf RJ, Williams ED. Phys Rev Lett 1987;58:2563.

[69] Bartelt NC, Williams ED, Phaneuf RJ, Yang Y, Das Sarma S. J Vac Sci Technol A 1989;7:1898.

[70] Phaneuf RJ, Bartelt NC, Williams ED, Swiech W, Bauer E. Phys Rev Lett 1993;71:2284.

[71] Rousset S, Berroir JM, Repain V, Garreau Y, Etgens VH, Lecoeur J, et al. Surf Sci 1999;443:265.

[72] Bonczek F, Engel T, Bauer E. Surf Sci 1980;97:595.

[73] Madey TE, Guan J, Nien C-H, Tao H-S, Dong C-Z, Campbell RA. Surf Rev Lett 1996;3:1315.

[74] Madey TE, Nien C-H, Pelhos K, Kolodziej JJ, Abdelrehim IM, Tao H-S. Surf Sci 1999;438:191.

[75] Fisher DS, Weeks JD. Phys Rev Lett 1983;50:1077.

[76] Lyuksyutov I, Naumovets AG, Prokrovsky V. Two-dimensional crystals. San Diego: Academic Press; 1992.

[77] Dieluweit S, Ibach H, Giesen M, Einstein TL. Phys Rev B 2003;67:121410(R).

[78] Stasevich TJ, Einstein TL, Zia RKP, Giesen M, Ibach H, Szalma F. Phys Rev B 2004;70:245404.

[79] Stasevich TJ, Einstein TL, Stolbov S. Phys Rev B 2006;73:115426.

[80] Stasevich TJ, Gebremariam H, Einstein TL, Giesen M, Steimer C, Ibach H. Phys Rev B 2005;71:245414.

[81] Zia RKP. J Stat Phys 1986;45:801.

[82] Avron JE, van Beijeren H, Schulman LS, Zia RKP. J Phys A Math Gen 1982;15:L81–6.

[83] Gallavotti G. Commun Math Phys 1972;27:103.

[84] Abraham DB, Reed P. Phys Rev Lett 1974;33:377.

[85] Abraham DB, Reed P. Commun Math Phys 1976;49:35.

[86] Kodambaka S, Khare SV, Petrov I, Greene JE. Surf Sci Rep 2006;60:55–77.

[87] Michely T, Krug J. Berlin: Springer; 2004 [Chapter 3].

[88] Stasevich TJ, Einstein TL. [SIAM-]Multiscale Model Simul 2007;6:90.

[89] Weeks JD. Private discussions, 2014.

[90] Liu F. Modeling and simulation of strain-mediated nanostructure formation on surface. In: Rieth M, Schommers W, editors. Handbook of theoretical and computational nanotechnology, vol. 4. American Scientific Publishers; 2006. p. 577–625.

[91] Müller B, Nedelmann L, Fischer B, Brune H, Barth JV, Kern K. Phys Rev Lett 1998;80:2642.

[92] Einstein TL. Appl Phys A 2007;87:375384 [cond-mat/0612311].

[93] Einstein TL, Richards HL, Cohen SD, Pierre-Louis O. Surface Sci 2001;493:460.

[94] Einstein TL. Interactions between adsorbate particles. In: Unertl WN, editor. Physical structure of solid surfaces. Handbook of surface science, vol. 1. Amsterdam: Elsevier; 1996. Holloway S, Richardson NV, series editors, 577–650.

[95] Giesen M. Prog. Surface Sci. 2001;68:1.

[96] Gruber E, Mullins WW. J Phys Chem Solids 1967;28:875.

[97] Fisher MPA, Fisher DS, Weeks JD. Phys Rev Lett 1982;48:368.

[98] Leamy HJ, Gilmer GH, Jackson KA. Statistical thermodynamics of clean surfaces. In: Blakely JM, editor. Surface physics of materials, vol. 1. New York: Academic Press; 1975. p. 121 [Chapter 3].

[99] Stasevich TJ. 2006 [Ph.D. dissertation]. University of Maryland [unpublished].

[100] de Gennes PG. J Chem Phys 1968;48:2257.

[101] Prokrovsky VL, Talapov AL. Phys Rev Lett 1979;42:65. Sov Phys-JETP 1980;51:134.

[102] Haldane FDM, Villain J. J Phys Paris 1981;42:1673.

[103] Schulz HJ, Halperin BI, Henley CL. Phys Rev B 1982;26:3797.

[104] Prokrovsky VL, Talapov AL. Theory of incommensurate crystals, soviet scientific reviews supplement series physics, vol. 1. Chur: Harwood Academic Publishers; 1984 [and references therein].

[105] Villain J. In: Riste T, editor. Ordering in strongly fluctuating condensed matter systems. New York: Plenum; 1980. p. 221.

[106] Akutsu Y, Akutsu N, Yamamoto T. Phys Rev Lett 1988;61:424.

[107] Jeong H-C, Weeks JD. Surf Sci 1999;432:101 [and references therein].

[108] Wang X-S, Goldberg JL, Bartelt NC, Einstein TL, Williams ED. Phys Rev Lett 1990;65:2430.

[109] Ihle T, Misbah C, Pierre-Louis O. Phys Rev B 1998;58:2289.

[110] Joós B, Einstein TL, Bartelt NC. Phys. Rev. B 1991;43:8153.

[111] Mehta ML. Random matrices. 3rd ed. New York: Academic; 2004.

[112] Dyson FJ. Statistical Theory of the Energy Levels of Complex Systems. III. J. Math. Phys. 1962;3:166.

[113] Bartelt NC, Einstein TL, Williams ED. Surf Sci 1990;240:L591.

[114] Calogero F. J Math Phys 1969;10:2191. 2197.

[115] Sutherland B. J Math Phys 1971;12:246. Phys Rev A 1971;4:2019.

[116] Dyson FJ. Commun. Math. Phys. 1970;19:235.

[117] Haake F. Quantum signatures of chaos. 2nd ed. Berlin: Springer; 1991.

[118] Guhr T, Müller-Groeling A, Weidenmüller HA. Phys. Rept 1998;299:189.

[119] Gebremariam H, Cohen SD, Richards HL, Einstein TL. Phys Rev B 2004;69:125404.

[120] Jayaprakash C, Saam WF. Phys Rev B 1984;30:3916.

[121] Andreev AF. Sov. Phys.-JETP 1982;53:1063 [Zh. Eksp. Teor. Phys 1981;80:2042].

[122] Jayaprakash C, Saam WF, Teitel S. Phys Rev Lett 1983;50:2017.

[123] Cabrera N, García N. Phys Rev B 1982;25:6057.

[124] Cabrera N. The equilibrium of crystal surfaces. Surf Sci 1964;2:320.

[125] Kardar M, Nelson DR. Phys Rev Lett 1985;55:1157.

[126] Dahmen SR, Wehefritz B, Albertini G. A novel exponent in the equilibrium shape of crystals. 1998. arXiv:cond-mat/9802152.

[127] Akutsu Y, Akutsu N, Yamamoto T. Universality of the tangential shape exponent at the facet edge of a crystal. 1998. arXiv:cond-mat/9803189.

[128] Akutsu Y, Akutsu N. Prog Theor Phys 2006;116:983.

[129] Nishino T, Okunishi K. J Phys Soc Jpn 1995;64:4084.

[130] Okunishi K, Hieida Y, Akutsu Y. Phys Rev B 1999;59:6806. 1999;60:R6953.

[131] Sato R, Akutsu Y. J Phys Soc Jpn 1995;64:3593.

[132] Carmi Y, Lipson SG, Polturak E. Phys Rev B 1987;36:1894.

[133] Rottman C, Wortis M, Heyraud JC, Métois JJ. Phys Rev Lett 1984;52:1009.

[134] Saénz JJ, García N. Surf Sci 1985;155:24.

[135] Surnev S, Arenhold K, Coenen P, Voigtländer B, Bonzel HP. J Vac Sci Technol A 1998;16:1059.

[136] Nowicki M, Bombis C, Emundts A, Bonzel HP, Wynblatt P. New J Phys 2002;4:60.

[137] Nowicki M, Bombis C, Emundts A, Bonzel HP, Wynblatt P. Eur Phys Lett 2002;59:239.

[138] Nowicki M, Bombis C, Emundts A, Bonzel HP. Phys Rev B 2003;67:075405.

[139] Bonzel HP, Nowicki M. Phys Rev B 2004;70:245430.

[140] Bonzel HP, Yu DK, Scheffler M. Appl Phys A 2007;87:391.

[141] Thürmer K, Reutt-Robey JE, Williams ED. Surf Sci 2003;537:123.

[142] Métois JJ, Heyraud JC. Surf Sci 1987;180:647.

[143] Bermond JM, Métois JJ, Heyraud JC, Floret F. Surf Sci 1998;416:430.

[144] Gladić J, Vučić Z, Lovrić D. J Cryst Growth 2002;242:517–32.

[145] Ferrari PL, Prähofer M, Spohn H. Phys Rev E 2004;69:035102.

[146] Pimpinelli A, Degawa M, Einstein TL, Williams ED. Surf Sci 2005;598:L355.

[147] Degawa M, Stasevich TJ, Cullen WG, Pimpinelli A, Einstein TL, Williams ED. Phys Rev Lett 2006;97:080601.

[148] Degawa M, Stasevich TJ, Pimpinelli A, Einstein TL, Williams ED. Surface Sci. 2007;601:3979 [Proc. ECOSS 2006].

[149] Einstein TL, Alberto Pimpinelli. J Statistical Phys 2014;155:1178. longer version posted at arXiv http://arxiv:1312.4910v1.

[150] Farnsworth HE, Schlier RE. J Chem Phys 1959;31:89.

[151] Hwang RQ, Williams ED, Park RL. Phys Rev B 1989;40:11716.

[152] Williams ED, Phaneuf RJ, Wei Jian, Bartelt NC, Einstein TL. Surface Sci 1993;294:219. Erratum 1994:310:451.

[153] Noh DY, Blum KI, Ramstad MJ, Birgeneau RJ. Phys Rev B 1991;44:10969.

[154] Noh DY, Blum KI, Ramstad MJ. Phys Rev B 1993;48:1612.

[155] Held GA, Goodstein DM, Brock JD. Phys Rev B 1995;51:7269.

[156] Noh DY, Liang KS, Hwu Y, Chandavarkar S. Surf Sci 1995;326:L455.

[157] Dietrich S, Haase A. Phys Rep 1995;260:1.

[158] Ocko B. Private discussion, 2014.

[159] Cahn JW. J de Physique 1982;43(C6):199–213. Proceedings of Conference on the Structure of Grain Boundaries, Caen, France.

[160] Somorjai GA, Van Hove MA. Prog Surf Sci 1989;30:201.

[161] Cheng W-C, Wynblatt P. Surf Sci 1994;302:185.

[162] Meltzman H, Chatain D, Avizemer D, Besmann TM, Kaplan WD. Acta Mater 2011;59:3473.

[163] Yoon M, Mochrie SGJ, Zehner DM, Watson GM, Gibbs D. Phys Rev B 1994;49:16702.

[164] Walko DA, Robinson IK. Phys Rev B 2001;64:045412.

[165] Szczepkowicz A, Ciszewski A, Bryl R, Oleksy C, Nien C-H, Wu Q, et al. Surf Sci 2005;599:55.

[166] Kalff M, Comsa G, Michely T. Phys Rev Lett 1998;81:1255.

[167] Stasevich TJ, Tao C, Cullen WG, Williams ED, Einstein TL. Phys Rev Lett 2009;102:085501.

[168] Wang Z, Wynblatt P. Surf Sci 1998;398:259.

[169] Handwerker CA, Vaudin MD, Blendell JE. J Phys Colloq 1988;49:C5-367.

[170] Emundts A, Bonzel HP, Wynblatt P, Thrmer K, Reutt-Robey J, Williams ED. Surf Sci 2001;481:13.

[171] Shimoni N, Ayal S, Millo O. Phys Rev B 2000;62:13147.

[172] Kukta RV, Peralta A, Kouris D. Phys Rev Lett 2002;88:186102.

[173] Prévot G, Croset B. Phys Rev Lett 2004;92:256104.

[174] Hecquet P. Surf Sci 2008;602:819.

[175] Wang G, Webb JF, Zi J. Surf Sci 2007;601:1944.

[176] Su WP, Schrieffer JR, Heeger AJ. Phys Rev Lett 1979;42:1698. Phys Rev B 1980;22:2099.

[177] Alerhand OL, Vanderbilt D, Meade RD, Joannopoulos JD. Phys Rev Lett 1988;61:1973.

[178] Copel M, Gustafsson T. Phys Rev Lett 1986;57:723.

[179] Peierls RF. Quantum theory of solids. Oxford: Clarendon; 1955. p. 108 [Also Fröhlich H. Proc R Soc A 1954;223:296].

[180] Ercolessi F, Bartolini A, Garofalo M, Parrinello M, Tosatti E. Surf Sci 1987;189/190:636.

[181] Tosatti E. Private communication, March 2014.

[182] Song S, Yoon M, Mochrie SGJ. Surf Sci 1995;334:153.

[183] Zuo J-K, Zhang T, Wendelken JF, Zehner DM. Phys Rev B 2001;63:033404.

[184] Shenoy VB, Ciobanu CV. Phys Rev B 2003;67(081402).

[185] Yamamoto M, Sudoh K, Iwasaki H, Williams ED. Phys Rev B 2010;82:115436.

[186] Ciobanu CV, Tambe DT, Shenoy VB, Wang CZ, Ho KM. Phys Rev B 2003;68:201302R.

[187] Sathiyanarayanan R, Hamouda ABH, Einstein TL. Phys Rev B 2009;80:153415.

[188] Lässig M. Phys Rev Lett 1996;77:526.

[189] Akutsu N. J Phys Condens Matter 2011;23:485004.

[190] Einstein TL, Schrieffer JR. Phys Rev B 1973;7:3629.

[191] Ruderman MA, Kittel C. Phys Rev 1954;96:99.

[192] Yosida K. Phys Rev 1957;106:893.

[193] Redfield AC, Zangwill A. Phys Rev B 1992;46:4289.

[194] Frohn J, Giesen M, Poensgen M, Wolf JF, Ibach H. Phys Rev Lett 1991;67:3543.

[195] Lau KH, Kohn W. Surf Sci 1978;75:69.

[196] Repp J, Moresco F, Meyer G, Rieder K-H, Hyldgaard P, Persson M. Phys Rev Lett 2000;85:2981.

[197] Hyldgaard P, Persson M. J Phys Condens Matter 2000;12:L13.

[198] Knorr N, Brune H, Epple M, Hirstein A, Schneider MA, Kern K. Phys Rev B 2002;65:115420.

[199] Hyldgaard P, Einstein TL. J Cryst Growth 2005;275:e1637 [cond-mat/0408645].

[200] Ashcroft NW, Mermin ND. Solid state physics. Cengage Learning; 1976.

[201] Crommie MF, Lutz CP, Eigler DM. Nature 1993;363:524. Science 1993;262:218.

[202] Kevan SD. Phys Rev B 1983;28:2268(R).

[203] Pai WW, Ozcomert JS, Bartelt NC, Einstein TL, Reutt-Robey JE. Surf Sci 1994;309:747.

[204] Liu SH, Hinnen C, van Huong CN, de Tacconi NR, Ho K-M. J Electroanal Chem 1984;176:325.

[205] Mugarza A, Schiller F, Kuntze J, Cordón J, Ruiz-Osés M, Ortega JE. J Phys Condens Matter 2006;18: S27.

[206] Li F, Allegretti F, Surnev S, Netzer FP. Surf Sci 2010;604:L43.

[207] Patrone PN, Einstein TL. Phys Rev B 2012;85:045429.

[208] Kodambaka S, Khare SV, Petrova V, Vailionis A, Petrov I, Greene JE. Surf Sci 2002;513:468474.

[209] Kodambaka S, Khare SV, Petrova V, Johnson DD, Petrov I, Greene JE. Phys Rev B 2003;67:035409.

[210] Stranski I. Z. Phys Chem Leipz 1928;136:259.

[211] Flytzani-Stephanopoulos M, Schmidt LD. Prog Surf Sci 1979;9:83.

[212] Rottman C, Wortis M. Phys Rep 1984;103:5979.

[214] Gibbs JW. Trans Conn Acad 1877;3:108–248. see Collected Works 1928, p. 343–524.

[215] Zia RKP. Anisotropic surface tension and equilibrium crystal shapes. In: Hu CK, editor. Progress in Statistical Mechanics. Singapore: World Scientific; 1988. p. 303–57.

[216] Weeks JD. In: Riste T, editor. Ordering in strongly fluctuating condensed matter systems. New York: Plenum; 1980. p. 293.

[217] Rottman C, Wortis M. Phys Rev B 1984;29:328.

[218] von Laue M. Z. Krist Min 1944;105:124.

[219] Andreev AF. Sov Phys-JETP 1982;53:1063.

[220] For a review of fermionic methods, see den Nijs M. In: Domb C, Lebowitz JL, editors. Phase transitions and critical phenomena, vol. 12. London: Academic; 1989.

[221] Williams ED, Bartelt NC. Thermodynamics and statistical mechanics of surfaces. In: Unertl WN, editor. Physical structure of solid surfaces. Holloway S, Richardson NV, editors. Handbook of surface science, vol. 1. Amsterdam: Elsevier; 1996. p. 51–99.

[222] Einstein TL, Pimpinelli A. Dynamical scaling implications of Ferrari, Prähofer, and Spohn's remarkable spatial scaling results for facet-edge fluctuations, arXiv 1312.4910.

[223] Song S, Mochrie SGJ. Phys Rev Lett 1994;73:995.

[224] Song S, Mochrie SGJ. Phys Rev B 1995;51:10068.

[225] Shimoni N, Ayal S, Millo O. Phys Rev B 2000;62:13147.

[226] Barreteau C, Raouafi F, Desjonquères MC, Spanjaard D. J Phys Condens Matter 2003;15:3171.

[227] Yu DK, Bonzel HP, Scheffler M. The stability of vicinal surfaces and the equilibrium crystal shape of Pb by first principles theory. New J Phys 2006;8:65.

[228] Daw MS, Foiles SM, Baskes MI. Mater Sci Rep 1993;9:251.